Met. O. 979

METEOROLOGICAL OFFICE

Scientific Paper No. 41

The Meteorological Office operational numerical weather prediction system

by R. S. BELL, B.A. and A. DICKINSON, Ph.D.

HER MAJESTY'S STATIONERY OFFICE

Met. O. 979

METEOROLOGICAL OFFICE

Scientific Paper No. 41

The Meteorological Office operational numerical weather prediction system

by R. S. BELL, B.A. and A. DICKINSON, Ph.D.

LONDON: HER MAJESTY'S STATIONERY OFFICE

U.D.C. 551.509.313

© *Crown copyright 1987*

First published 1987

ISBN 011 400354 8

Contents

	Page
Partial list of symbols	iv
Summary	1
1. Introduction	1
2. Analysis of data	4
3. Assimilation	14
4. The forecast equations	20
5. The integration scheme	21
6. Dynamic precipitation	26
7. Deep convection	27
8. Surface and boundary layer	35
9. Radiation	42
10. Gravity-wave drag	51
11. Stability and zonal filtering	54
12. Lateral boundary conditions and the treatment of the poles	57
Acknowledgements	58
Bibliography	59

a	suffix for analysed value
a	radius of the earth
A	operator denoting adjustment step terms in the model equations
A_E	entrainment factor
A_λ, A_ϕ	adjustment terms in the model equations
A_*	accumulated precipitation at the surface
$A_{i\omega}$	absorption by gas i at frequency ω
b	suffix for background value
b	excess buoyancy parameter for convection
B	operator denoting physical parametrization terms and advection terms in the model equations
$B_\omega(T)$	Planck function
c_p	specific heat capacity of dry air at constant pressure
C	Stefan's constant
C_D, C_H, C_E	bulk transfer coefficients for momentum (C_D), heat (C_H), and moisture (C_E)
C_{base}, C_{top}	cloud base and top
D	divergence
$\mathrm{D_d}$	operator denoting divergence diffusion term
D_f	diffusion factor
D_k	convective cloud depth
E	root-mean-square error
E_m	evaporation per unit mass at level m
E_n	buoyancy
e	eccentricity of earth's orbit
e'	water vapour partial pressure
F_u, F_v, F_θ, F_q	vertical fluxes of momentum, heat and moisture
f	Coriolis parameter $2\Omega \sin\phi$
f_X	stability function used in definition of vertical diffusion coefficients for variable X
$\mathscr{F}_u$, $\mathscr{F}_v$, $\mathscr{F}_\theta$, $\mathscr{F}_q$	sources and sinks of momentum, heat and moisture
G	operator denoting geostrophic wind increment terms
g	acceleration due to gravity
g	suffix for grid-point value
H	operator denoting hydrostatic temperature increment terms
H_V	sub-grid-scale variance of orography
H_*	surface sensible heat flux
i	suffix for horizontal grid-point or observation point index
I, I^∞, I^C, $I^\uparrow$, $I^\downarrow$	long-wave radiation fluxes, total, clear sky, cloud, upward and downward
J	convective rainfall amounts
J_{base}	convective rainfall amounts from base of convective cloud
j	suffix for horizontal grid-point or observation point index
K_X	diffusion coefficient for variable X
k	Kármán's constant

k	vertical grid-point index ($k = 1$ denotes lowest level)
L_c, L_f	latent heats of condensation (either with respect to water or ice, as appropriate) and fusion
L	latent heat of evaporation
$\mathscr{L}$	Monin–Obukhov length scale
ℓ, ℓ_A	mixing length, asymptotic mixing length
M_I, M_{MIN}, M_k	initial, minimum and level k values of vertical mass flux in the convective plume
M	soil moisture content
m	model level
N	time period
n	suffix for time level
o	suffix for observed value
P_k	precipitation per unit mass at level k
p	pressure $= \sigma p_*$
p_*	pressure at earth's surface as represented by model orography
Q, Q_C, Q_L, Q_M, Q_H	total, convective, low, medium and high cloud amounts
Q_*	latent heat flux due to surface evaporation
q	specific humidity
q_s	saturation specific humidity
R	gas constant for dry air
Ri	local Richardson number
$(Ri)_B$	bulk Richardson number
R_ℓ	local convective rain rate
R_v	gas constant for water vapour
R_*	surface net radiation
$\mathscr{R}_k$	net radiative flux at level k
S	incoming solar radiation
S_p	solar constant at perihelion
T	temperature $= \theta(p/1000)^\kappa$
T_v	virtual temperature
T_*	surface temperature
t	time
U	relative humidity $= q/q_s \times 100$
u	zonal wind component
u'	zonal wind component along x axis using Cartesian coordinates
$\mathbf{v}$	vector wind
v	meridional wind component
v'	meridional wind component along y axis using Cartesian coordinates
W_1, W_2, W_3, W_4	scaling terms in the adjustment step for winds
W_i	optimum interpolation weight for observation i
W_*	large-scale precipitation rate
w_i	pressure scaling factor for gas i when calculating effective optical depth
$\mathbf{X}$	vector of model variables
X^n	generalized variable u, v, q or p_* at time level n
X^P	cloud water mixing ratio

X_m	magnification factor to account for change in atmospheric path length as zenith angle increases
x	suffix for local Cartesian coordinate
$x_{i\omega}$	extinction coefficient for gas i at frequency ω
Y	generalized variable
y	suffix for local Cartesian coordinate
y_i	optical path length for gas i
$\bar{y}$	effective optical depth, pressure weighted
z	height
z_0	roughness length
z_b	boundary-layer depth
α	albedo
α_{ij}	angle between $\mathbf{r}_{ij}$ and latitude at point i
β	coefficient of reflection of gravity waves
β_i	reflectivity of cloud type i
γ_g	scaling factor for geostrophic wind increments
γ_h	scaling factor for hydrostatic temperature increments
$\gamma_{i\omega}$	flux transmittance for gas i at frequency ω
γ	surface resistance to evaporation
γ_k	multiplying factor dependent on whether a convective parcel is saturated in layer k. $\gamma_k = 1$ if the parcel is saturated, otherwise $\gamma_k = 0$.
γ_s	safety factor used to scale the amplification factor in linear stability analysis
δ_k	detrainment rate due to forcing at level k
δ	solar declination
ε	ratio of molecular weight of water and dry air
ε^X	difference from truth for model variable X
ε_k	entrainment rate at level k
ε_i, $\bar{\varepsilon}_i$	partial emissivity, partial absorptivity
ζ	vorticity
η_k	detrainment due to mixing at level k
θ	potential temperature
θ_*	surface potential temperature
θ_v	virtual potential temperature $= \theta(1+0.61q)$
κ	R/c_p power used in Exner function
λ	longitude
λ'	wavelength
Λ	transmissivity of the cloud
ν	water vapour absorber amount
ξ	solar zenith angle
ξ_{ij}	angle subtended at earth's centre by points i, j
Π	Exner function $= (p_*/1000)^\kappa$
ρ	density of air
ρ_*	density of air at surface

$\rho_i(z)$	density of gas i at height z
σ	vertical coordinate $= p/p_*$
$\dot{\sigma}$	vertical velocity $\dfrac{d\sigma}{dt}$
$\underline{\tau}$	gravity-wave momentum flux
$\overline{\tau}$	transmissivity
τ_*	typical surface momentum flux
τ_0	hour angle
ϕ	latitude
χ	relaxation coefficient for scaling assimilation increment
ψ_M, ψ_H	Monin–Obukhov similarity functions
Φ	geopotential $= gz$
Φ_*	geopotential at surface of the earth
ω	frequency
Ω_p	angular distance of earth from perihelion
Ω	magnitude of earth's angular velocity
$\overline{A}^x$	$\{A(x + \Delta x/2) + A(x - \Delta x/2)\}/2$
δ_x^A	$\{A(x + \Delta x/2) + A(x - \Delta x/2)\}/\Delta x$
Δx	increment in x
$\Delta \mathbf{X}$	calculated corrections to vector of model fields
$\Delta A_{k+\frac{1}{2}}$	$A_{k+1} - A_k$
$\delta/\delta x$	partial derivative with respect to x
∇	lateral gradient operator

The Meteorological Office operational numerical weather prediction system

by R. S. Bell, B.A. and A. Dickinson, Ph.D.

SUMMARY

This paper gives a description of the numerical weather prediction system which is used operationally in the Meteorological Office to provide guidance to forecasters on time-scales of 12 hours to 6 days. The model described in this paper was introduced during the autumn of 1982 and replaced an earlier model which is described in Burridge and Gadd (1977). This paper details both the global coarse-mesh version of the model and also a limited-area fine-mesh version. The components of the data assimilation scheme, including data preparation, quality control, analysis and assimilation are dealt with in the first few sections. Following that, the forecast model is described, including details of the basic system of equations, the integration scheme and the physical and sub-grid-scale processes which are represented in the model.

1. INTRODUCTION

In August 1982, after 10 years of service, the Meteorological Office 10-level numerical weather prediction model which was described in Burridge and Gadd (1977) was withdrawn from daily operational use. Its replacement, which is described in this paper, was designed to take advantage of the advances which have been made in several fields during the past decade. A large increase in the available computer power has allowed the implementation of a scheme which is more advanced in many respects and gives global coverage on a higher resolution than the old model.

The data assimilation scheme has been designed to cope with today's complex mix of observing systems which are increasingly asynoptic and heterogeneous as regards reliability and accuracy, as the trend towards remote sensing and automatic instrumentation has increased. The philosophy of analysing the observations for a specific instant has been abandoned in favour of a scheme whereby the observational data (or rather their differences from values predicted by the forecast model), interpolated to model grid points, are used to guide the model towards the observed state as it is integrated over a so-called assimilation period. This technique evolved from a suggestion by Lorenc (1976) and proved successful in a semi-operational environment during the First GARP Global Experiment (FGGE) in 1979. The present scheme described below in sections 2 and 3 has its origins in the system developed for FGGE which has been described by Lyne *et al.* (1982). Figure 1 illustrates the assimilation cycle. Section 2 describes how the observations are interpreted, quality controlled and analysed. Section 3 follows by describing how the selected observations are inserted into the forecast model during the assimilation period preceding the nominal observation time.

The design of the new forecast model followed a period of research aimed at identifying the most important ingredients for a successful short-to-medium-range prediction model. The results of this research (Cullen *et al.* 1981) suggested that none of the possible discretization techniques, that is finite difference, spectral or finite element, showed any clear advantage over the others, and the design strategy was thus to implement a simple economical model with as high a resolution as resources would allow. A split-explicit finite-difference scheme (Gadd 1978a) is used to integrate the governing prognostic

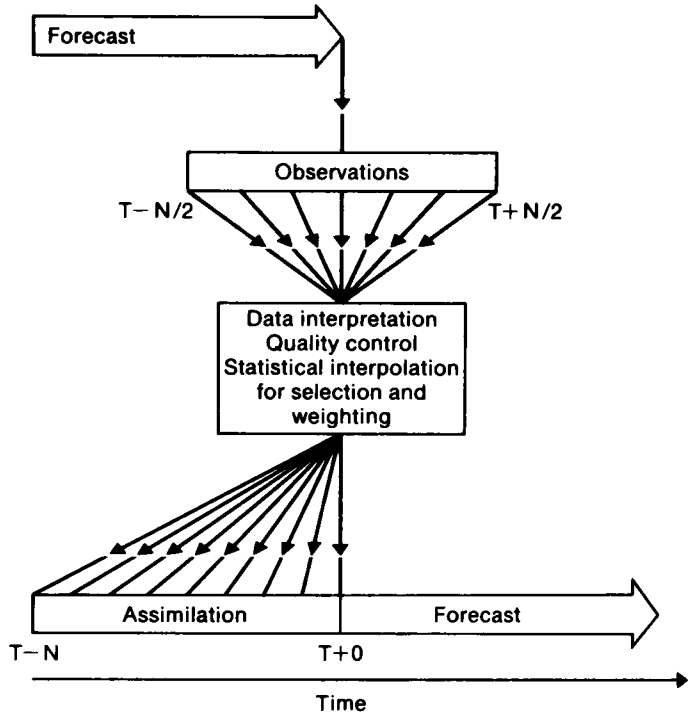

FIGURE 1. Schematic diagram of assimilation cycle

equations for momentum, temperature and humidity together with the continuity and hydrostatic equations. A full description of the equations and their solution is given in sections 4 and 5. Sections 6 to 10 detail the physical and sub-grid-scale processes which are included in the model. The techniques used for parametrizing precipitation, radiation and the vertical transfer of heat, moisture and momentum through the atmospheric boundary layer, were developed in recent years for use in the Meteorological Office's 11-layer general circulation model (Slingo A. 1985).

To enable global coverage to be achieved conveniently, the equations are defined on a latitude–longitude grid. A limited-area version of the model with a finer mesh also uses a latitude–longitude grid. The global model has a mesh with grid lengths $\Delta\lambda = 1.875°$ along lines of latitude and $\Delta\phi = 1.5°$ along lines of longitude. This means that there are 192 points around each latitude circle and 121 points from North Pole to South Pole. The limited-area fine-mesh version of the model has a resolution twice that of the coarse-mesh model ($\Delta\lambda = 0.9375°$, $\Delta\phi = 0.75°$). The integration area is shown in Figure 2. It is enclosed by longitude lines 80.625°W and 39.375°E, and by latitude lines 79.5°N and 30°N which gives 129 points east–west and 67 points north–south. The variables are horizontally staggered using the arrangement of the so-called 'B' grid (Arakawa 1966). This is illustrated in Figure 3. Thus the zonal wind component (u) and the meridional wind component (v) are held at points $(i + \frac{1}{2})\Delta\lambda, (j + \frac{1}{2})\Delta\phi$, where i and j are horizontal grid-point indices, whilst the remaining variables, surface pressure (p_*), potential temperature (θ), specific humidity (q) together with the diagnostic quantities, vertical velocity ($\dot{\sigma}$) and geopotential (Φ), are held at the points $(i\Delta\lambda, j\Delta\phi)$. In the vertical a sigma coordinate system, defined by $\sigma = p/p_*$ where p is pressure

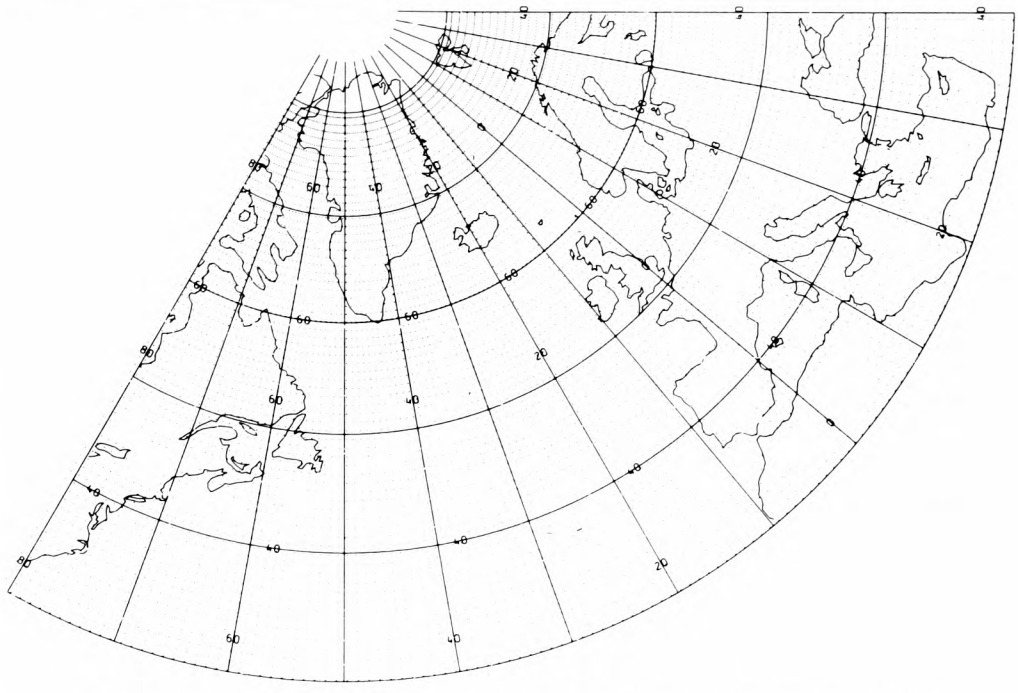

FIGURE 2. The integration area of the operational fine-mesh model

and p_* is surface pressure (Phillips 1957), is used. Both versions of the model have 15 unequally spaced σ-levels which are positioned to give higher resolution in the boundary layer and in the vicinity of the tropopause and jet streams. The variables, u, v, θ, q, Φ are held at the levels σ_k, where k is the vertical grid-point index, while the vertical velocity is held at the intermediate level $\sigma_{k+\frac{1}{2}}$. The σ-level values are given in Table I.

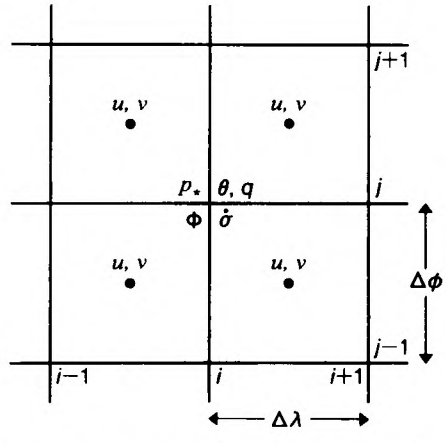

FIGURE 3. Arrangement of variables on the 'B' grid

TABLE I. *The σ-levels used by the operational forecast models*

Number	Full-level	Half-level
		0.013
15	0.025	0.042
14	0.065	0.098
13	0.125	0.156
12	0.190	0.228
11	0.250	0.273
10	0.310	0.350
9	0.390	0.433
8	0.490	0.552
7	0.590	0.630
6	0.690	0.754
5	0.790	0.827
4	0.870	0.914
3	0.935	0.956
2	0.975	0.994
1	0.997	

Special measures are required to ensure stability as the meridians converge near the pole and these are discussed in section 11. The limited-area fine-mesh version of the model requires lateral boundary information. These boundary considerations are discussed further in section 12.

A 6-hour cycle has been adopted for the global coarse-mesh data assimilation scheme, with analyses at 06, 12, 18 and 00 GMT. Forecasts for 6 days ahead are computed twice daily from the midday and midnight analyses. The fine-mesh data assimilation cycle consists of four analyses at 3-hour intervals commencing from an interpolated coarse-mesh analysis and leading up to a fine-mesh forecast which is produced twice daily for 36 hours ahead.

A more detailed account of the research leading to the design of the new system is given by Gilchrist and White (1982). Since its introduction the new system has been subject to a continuous process of development. Research is currently in progress on many aspects and further significant improvements are envisaged in the future. This paper documents the version which is operational at the time of writing and cannot be considered as a final statement.

2. ANALYSIS OF DATA

The analysis of data consists of three stages: preprocessing, quality control, and calculation of weights. An optimal interpolation scheme is used for both quality control and calculation of weights, so we describe the equations used in section 2.2 before discussing the quality control. It should be noted that an interpolation grid-point analysis is not produced; only the weights are used in the assimilation of the observations, which is described in section 3.

2.1. *Data preprocessing*

Coded observations arrive at the Meteorological Office continuously via the Global Telecommunication System. The observations are of different variables and may relate to one or many levels of the atmosphere. Before being analysed, they must be processed so that they can be more readily used by the analysis scheme. The variables analysed must in general be the same as the model's prognostic variables, namely surface pressure, potential temperature, and horizontal wind components. An exception is moisture which is more conveniently analysed as relative humidity. The precise way in which the reported observations are prepared for use by the analysis is clearly important. Woodage (1985) explains the procedure in some detail and only a brief description will be given here. Table II lists the main observation types together with details of the variables and level to be analysed. For many observation types a straightforward conversion of variables is all that is required, using standard formulae. Two conversions which require rather more care are the interpretation of surface pressure information and the preprocessing of radiosonde data.

TABLE II. *Observations used by the data assimilation scheme*

Type of observation	Variable	Levels
Surface land	p_*	$\sigma = 1$
Surface ship	p_*, U, $\mathbf{v}$	$\sigma = 1$
Drifting buoy	p_*	$\sigma = 1$
Upper air TEMP (radiosonde wind, temperature)	p_*, U, θ, $\mathbf{v}$	Model σ-levels
Upper air PILOT (radiosonde wind only)	$\mathbf{v}$	Model σ-levels
SATEM (satellite temperature sounding)	θ	Mid-point of reported layers
SATOB (cloud-track wind)	$\mathbf{v}$	As reported
AIREP (aircraft report)	θ, $\mathbf{v}$	As reported
BOGUS (manually generated observations)	p_*, U, θ, $\mathbf{v}$	Mid-point standard levels

By World Meteorological Organization convention surface pressure observations are reported as the pressure at mean sea level (pmsl) (derived using a standard formula from the measured station-level pressure), although some high-level stations report station-level pressure or the height of the nearest standard pressure level. The analysis requires a value for the pressure at the ground level as depicted within the model. This involves an extrapolation and assumptions are required about the temperature structure of the layer between the model's ground surface and mean sea level. The assumption made is that a constant

International Civil Aviation Organization lapse rate ($0.0065\,K\,m^{-1}$) exists and the temperature at the lowest level outside the boundary layer ($\sigma = 0.79$) obtained from a model prediction from an early time is taken as a reference. This method is the inverse of the technique used for converting p_* to pmsl when producing output charts of model forecasts for presentation to the forecaster.

The interpretation of radiosonde data involves a pre-analysis of each ascent. The radiosondes provide data at fixed standard levels and also at sufficient significant levels to enable all the observed fine detail to be reconstructed as required. There may be more than 50 levels reported and much of the observed detail cannot be resolved by the model. The radiosonde ascent is reinterpreted in terms of layer values appropriate to the resolution of the model at any given level. To avoid including incorrect data in the averaging process involved, a preliminary quality-control step checks the internal consistency of a report including an examination of lapse rates and wind shears. In addition to this averaging procedure, the temperatures reported from radiosondes are corrected for systematic errors on a station-by-station basis.

It is also evident from Table II that certain observed variables are not presented to the analysis. In particular no use is made of the wind, temperature or humidity data from surface land stations; it is considered that local anomalies would render such observations unrepresentative of the atmosphere on the scale of the model. Another restriction relating to the use of surface data occurs in data-dense areas where a limit is placed on the maximum observation density by using only stations from a predetermined reduced list. Another restriction on data usage which is worth mentioning is that satellite temperature sounding data are used only over the sea areas.

In addition to the data conversion discussed above, the data preparation stage also involves arranging the data in 1.5° latitude bands starting at the North Pole. Within these bands the observations are ordered in terms of increasing longitude. The observation data file is then formatted in a special manner to take advantage of the vector processing architecture of the Control Data Corporation Cyber 205 supercomputer which is used for operational forecasting at the Meteorological Office.

2.2 *Optimal interpolation scheme*

Optimal interpolation is used to interpolate values at each observation position for quality control and to calculate weights for the interpolation of observations to model grid points (Gandin 1963, Rutherford 1972). We describe here the grid-point scheme; that used for quality control is essentially the same. The careful interpolation of data has been found to be a very necessary requirement for its adequate assimilation (Ghil *et al.* 1979). Differences between observed values and a background or first-guess field are calculated at observation points and are then linearly interpolated to model grid points.

$$X_g^a - X_g^b = \sum_i W_i (X_i^o - X_i^b) \qquad \ldots (2.1)$$

Here X is the variable to be interpolated, subscripts g and i refer to grid and observation points respectively, and superscripts a, b and o refer to analysed, background and observed values. Although equation (2.1) is univariate, optimal interpolation in its most general form

can be multivariate with the analysed variable being of a different type to the observations (Lorenc 1981).

The analysis is optimal in the sense that the weights W_i are chosen so that the expected error $E_g^{a^2}$ variance of the interpolated value as given by equation (2.2) is a minimum

$$\begin{aligned} E_g^{a^2} &= \langle (X_g^a - X_g^{tr})^2 \rangle \\ &= \langle \varepsilon_g^{a^2} \rangle \\ &= \langle \{ \varepsilon_g^b + \sum_i W_i (\varepsilon_i^o - \varepsilon_i^b) \}^2 \rangle. \end{aligned} \quad \ldots (2.2)$$

A superscript tr denotes the true value, ε the error and $\langle \ \rangle$ an ensemble mean. It can be shown that the W_i must satisfy the following set of simultaneous equations, the number of equations being equal to the number of observations used in interpolating to a model grid point.

$$\sum_i W_i (\langle \varepsilon_i^o \varepsilon_j^o \rangle + \langle \varepsilon_i^b \varepsilon_j^b \rangle - \langle \varepsilon_i^o \varepsilon_j^b \rangle - \langle \varepsilon_j^o \varepsilon_i^b \rangle) = \langle \varepsilon_j^b \varepsilon_g^b \rangle - \langle \varepsilon_j^o \varepsilon_g^b \rangle \quad \ldots (2.3)$$

On the assumption that observational errors are unbiased and not correlated with the background values, equation (2.3) reduces to

$$\sum_i W_i (\langle \varepsilon_i^o \varepsilon_j^o \rangle + \langle \varepsilon_i^b \varepsilon_j^b \rangle) = \langle \varepsilon_j^b \varepsilon_g^b \rangle \quad \ldots (2.4)$$

where $\langle \varepsilon^o \varepsilon^o \rangle$ and $\langle \varepsilon^b \varepsilon^b \rangle$ are the observational and background field error covariances respectively. The expected analysis error may then be shown to be

$$E_g^{a^2} = E_g^{b^2} - \sum_i W_i \langle \varepsilon_i^b \varepsilon_g^b \rangle. \quad \ldots (2.5)$$

Aspects of the analysis stage are described in more detail in the following subsections.

2.3. *Errors and error correlations*

The root-mean-square observational errors E^o are specified in a look-up table and vary with respect to observation type and with height. Values are specified on standard pressure levels and there is no interpolation in the vertical; the value taken is that of the standard pressure level nearest the observation. For some observations, the values are modified according to past reliability. Current values of observation errors for some of the more important observation types at selected pressure levels are given in Tables III, IV and V. These error levels are based on accumulated statistics of the differences between the observations and the background values.

TABLE III. *Surface pressure observation error (mb)*

	Error
Surface land station	1.0
Surface ship	1.0
Drifting buoy	1.6

TABLE IV. *Potential temperature observation error (K)*

	Error		
	Radiosonde	Satellite sounding	Aircraft report
1000 mb	1.8	2.2	—
700 mb	1.3	1.9	2.7
500 mb	1.3	2.0	2.9
300 mb	2.0	2.5	3.4
100 mb	3.1	3.1	4.6
50 mb	4.0	3.8	—

TABLE V. *Wind component observation error ($m\ s^{-1}$)*

	Error			
	Radiosonde	Surface ship	Aircraft report	Satellite cloud wind
1000 mb/surface	1.8	2.5	—	2.5
700 mb	1.8	—	5.5	4.5
500 mb	2.2	—	5.5	4.5
300 mb	2.9	—	5.5	6.5
100 mb	2.5	—	5.5	—
50 mb	2.5	—	—	—

The root-mean-square background field errors E^b are carried in a separate data file and are specified on a coarse 5° latitude–longitude grid and on six pressure levels in the vertical (900, 700, 500, 300, 100 and 50 mb). Values are calculated at observation points and analysis grid points by bi-linear interpolation in the horizontal and by linear interpolation in log (pressure) in the vertical. Values on pressure levels outside the range of those of the error data set are found by extrapolation. Some of the values currently being used are given in Tables VI, VII and VIII. The first-guess error fields are based on mean square values of forecast minus verifying analysis with additional amendments to ensure consistency between them and the chosen observation errors and observation minus first-guess statistics.

TABLE VI. *Example of first-guess error for surface pressure (mb)*

Latitude	Error (max./min./mean)
70°N	3.0/1.3/1.9
30°N	2.4/1.1/1.4
30°S	2.5/1.3/1.6
70°S	4.3/2.4/2.9

TABLE VII. *Example of first-guess error for potential temperature (K)*

	Error (max./min./mean)		
Latitude	900 mb	500 mb	300 mb
70°N	2.6/1.6/1.9	2.5/1.9/2.2	3.3/2.5/2.8
30°N	2.8/1.0/1.4	3.4/1.1/1.6	3.9/1.7/2.5
30°S	3.5/1.0/1.3	2.5/1.0/1.3	3.1/1.6/2.2
70°S	3.3/2.2/2.8	3.4/2.1/2.8	5.3/3.6/4.7

TABLE VIII. *Example of first-guess error for wind component ($m\ s^{-1}$)*

	Error (max./min./mean)		
Latitude	900 mb	500 mb	300 mb
70°N	5.5/3.4/4.0	4.6/3.4/3.9	5.2/3.8/4.4
30°N	10.0/4.3/5.6	11.2/3.6/5.2	11.0/4.8/7.1
30°S	13.5/4.1/5.6	9.1/3.4/4.5	9.8/5.0/6.8
70°S	7.2/4.8/6.0	6.2/3.8/5.2	8.3/5.7/7.4

The observational error covariances in equation (2.4) are expressed as products of root-mean-square errors and error correlations (μ)

$$\langle \varepsilon_i^o\ \varepsilon_j^o \rangle = E_i^o\ \mu_{ij}^o\ E_j^o. \qquad \ldots (2.6)$$

For most types of observations the error correlations are zero, only being significant for several observations of a variable from a single instrument.

Observational error correlations are specified as analytic functions of distance.

Only temperature data derived from satellite observations (SATEMs) are assumed to have correlated errors. The correlation function for these is defined as

$$\mu_{ij}^o = \exp\left\{-400\ \xi_{ij}^2 - 1.83\,|\ln(p_i/p_j)|\right\} \qquad \ldots (2.7)$$

where ξ_{ij} is the angle in radians subtended at the earth's centre by points i and j, and p_i and p_j are their pressure levels. No estimate of the correlation of errors in the vertical for data from a single upper-air observation is needed since only one piece of information is selected from each observation for a given analysis level.

The background field error covariances in equation (2.4) are also expressed as products of root-mean-square errors and error correlations

$$\langle \varepsilon_i^b\ \varepsilon_j^b \rangle = E_i^b\ \mu_{ij}^b\ E_j^b. \qquad \ldots (2.8)$$

Analytic functions are again specified for the correlations but are based on a single height–height error correlation function

$$\mu(\Phi_i, \Phi_j) = \exp\{-a_0 r_{ij}^2 - b_0 \ln^2(p_i/p_j)\} \quad \ldots (2.9)$$

where a_0 and b_0 are parameters defining the width of the horizontal and vertical correlation functions for background errors respectively, $a_0 = 3.3 \times 10^{-12}$ m^{-2}, $b_0 = 3$ and r_{ij} is the horizontal distance from the ith to the jth observation. This function was chosen because it exhibits the correct qualitative behaviour of the distribution of expected error, and because it leads to a positive definite system of simultaneous equations (2.4) ensuring non-singularity. Error correlation functions for other variables can be derived from equation (2.9) as described below. This procedure has the advantage that constraints such as geostrophy can be enforced in deriving the error covariances for full multivariate analysis (Lorenc 1981).

Let ε^X be the background error for the model variable X, E^X its root-mean-square value, and $\mu(X_i, Y_j)$ the correlation between the errors of variables X and Y at points i and j respectively. Then equation (2.8) for the error covariances becomes

$$\langle \varepsilon_i^X \varepsilon_j^Y \rangle = E_i^X \mu(X_i, Y_j) E_j^Y. \quad \ldots (2.10)$$

The functional forms of the error covariances between the surface pressure (p_*), potential temperature (θ) and the westerly (u) and southerly (v) wind components are all derived from the single height–height error correlation function defined in equation (2.9). This is achieved by assuming that hydrostatic and geostrophic relationships hold for the error fields. Thus if Φ is the geopotential

$$\left.\begin{aligned} \frac{\varepsilon_i^p}{p_i} &= -\frac{\varepsilon_i^\Phi}{RT_i} \quad \text{(isothermal atmosphere)} \\ \varepsilon_i^\theta &= \frac{1000^\kappa}{R} \exp\{-\kappa \ln(p_i)\} \frac{\partial \varepsilon_i^\Phi}{\partial \ln p_i} \\ \varepsilon_i^{u'} &= \frac{G_i}{f_i} \frac{\partial \varepsilon_i^\Phi}{\partial y} \\ \varepsilon_i^{v'} &= -\frac{G_i}{f_i} \frac{\partial \varepsilon_i^\Phi}{\partial x} \end{aligned}\right\} \quad \ldots (2.11)$$

where R is the gas constant for dry air, T is temperature, κ the R/c_p power used in the Exner function, x and y are local Cartesian coordinates, u' and v' the respective velocity components, f is the Coriolis parameter and G a parameter between 0 and 1 defining the degree of geostrophic balance. To enable the results to apply in the equatorial region it is assumed that the ratio G/f remains finite and non-zero in that area.

The following formulae for calculating univariate covariance functions can then be derived:

$$\left.\begin{aligned}
\langle \varepsilon_i^p \, \varepsilon_j^p \rangle &= \frac{p_i \, p_j}{R^2 \, T_i \, T_j} \langle \varepsilon_i^\Phi \, \varepsilon_j^\Phi \rangle \quad \text{(isothermal atmosphere)} \\
\langle \varepsilon_i^\theta \, \varepsilon_j^\theta \rangle &= \frac{1000^{2\kappa}}{R^2} \exp \{ -\kappa \ln (p_i \, p_j) \} \frac{\partial^2 \langle \varepsilon_i^\Phi \, \varepsilon_j^\Phi \rangle}{\partial \ln p_i \, \partial \ln p_j} \\
\langle \varepsilon_i^{u'} \, \varepsilon_j^{u'} \rangle &= \frac{G_i \, G_j}{f_i f_j} \frac{\partial^2 \langle \varepsilon_i^\Phi \, \varepsilon_j^\Phi \rangle}{\partial y_i \, \partial y_j} \\
\langle \varepsilon_i^{u'} \, \varepsilon_j^{v'} \rangle &= -\frac{G_i \, G_j}{f_i f_j} \frac{\partial^2 \langle \varepsilon_i^\Phi \, \varepsilon_j^\Phi \rangle}{\partial y_i \, \partial x_j} \\
\langle \varepsilon_i^{v'} \, \varepsilon_j^{u'} \rangle &= -\frac{G_i \, G_j}{f_i f_j} \frac{\partial^2 \langle \varepsilon_i^\Phi \, \varepsilon_j^\Phi \rangle}{\partial x_i \, \partial y_j} \\
\langle \varepsilon_i^{v'} \, \varepsilon_j^{v'} \rangle &= \frac{G_i \, G_j}{f_i f_j} \frac{\partial^2 \langle \varepsilon_i^\Phi \, \varepsilon_j^\Phi \rangle}{\partial x_i \, \partial x_j}
\end{aligned}\right\} \quad \ldots (2.12)$$

If the pressure–pressure error correlations are confined to surface pressure then the assumption of an isothermal atmosphere is well justified. In order that the covariances are hydrostatically and geostrophically linked it is further assumed that:

$$\left.\begin{aligned}
E_i^{p^*} &= E_i^\Phi \frac{p_{*i}}{R T_{*i}} \\
E_i^\theta &= E_i^\Phi \frac{1000^\kappa}{R} \exp (-\kappa \ln p_i) \sqrt{(2b_0)} \\
E_i^u = E_i^{u'} &= E_i^{v'} = E_i^\Phi \frac{G_i}{f_i} \sqrt{(2a_0)}
\end{aligned}\right\} \quad \ldots (2.13)$$

where the parameters a_0 and b_0 are those used in equation (2.9) defining the height–height error correlation function. Although the wind and temperature errors in the background field error file are specified independently, their values in middle and high latitudes are adjusted through these relations to satisfy the constraints approximately.

In calculating the weights for any one grid-point variable the same values of the error in the background field are used for each of the selected observation points. If this were not so, then the necessary condition of positive definiteness in the simultaneous equations could not be guaranteed. This is consistent with ignoring the horizontal derivatives of E^Φ in the following derivation.

The error covariances can now be derived as

$$\left.\begin{aligned}
\langle \varepsilon_i^{\Phi}\, \varepsilon_j^{\Phi} \rangle &= E_i^{\Phi}\, E_j^{\Phi}\, \mu(\Phi_i, \Phi_j) \\
\langle \varepsilon_i^{p^*}\, \varepsilon_j^{p^*} \rangle &= E_i^{p^*}\, E_j^{p^*}\, \mu(\Phi_i, \Phi_j) \\
\langle \varepsilon_i^{\theta}\, \varepsilon_j^{\theta} \rangle &= E_i^{\theta}\, E_j^{\theta} \{1 - 2b_0 \ln^2 (p_i/p_j)\}\, \mu(\Phi_i, \Phi_j) \\
\langle \varepsilon_i^{u'}\, \varepsilon_j^{u'} \rangle &= E_i^{u}\, E_j^{u} \{1 - 2a_0 (y_i - y_j)^2\}\, \mu(\Phi_i, \Phi_j) \\
\langle \varepsilon_i^{u'}\, \varepsilon_j^{v'} \rangle = \langle \varepsilon_i^{v'}\, \varepsilon_j^{u'} \rangle &= 2a_0\, E_i^{u}\, E_j^{u} (x_i - x_j)(y_i - y_j)\, \mu(\Phi_i, \Phi_j) \\
\langle \varepsilon_i^{v'}\, \varepsilon_j^{v'} \rangle &= E_i^{u}\, E_j^{u} \{1 - 2a_0 (x_i - x_j)^2\}\, \mu(\Phi_i, \Phi_j)
\end{aligned}\right\} \quad \ldots (2.14)$$

where $\mu(\Phi_i, \Phi_j)$ is defined by equation (2.9) with $r_{ij}^2 = (x_i - x_j)^2 + (y_i - y_j)^2$. The covariances for the westerly (u) and southerly (v) components of wind are related to the local components by

$$\left.\begin{aligned}
\langle \varepsilon_i^{u}\, \varepsilon_j^{u} \rangle &= \cos\alpha_{ij} \cos\alpha_{ji} \langle \varepsilon_i^{u'}\, \varepsilon_j^{u'} \rangle + \sin\alpha_{ij} \sin\alpha_{ji} \langle \varepsilon_i^{v'}\, \varepsilon_j^{v'} \rangle \\
\langle \varepsilon_i^{u}\, \varepsilon_j^{v} \rangle &= \cos\alpha_{ij} \sin\alpha_{ji} \langle \varepsilon_i^{u'}\, \varepsilon_j^{u'} \rangle - \sin\alpha_{ij} \cos\alpha_{ji} \langle \varepsilon_i^{v'}\, \varepsilon_j^{v'} \rangle \\
\langle \varepsilon_i^{v}\, \varepsilon_j^{u} \rangle &= \sin\alpha_{ij} \cos\alpha_{ji} \langle \varepsilon_i^{u'}\, \varepsilon_j^{u'} \rangle - \cos\alpha_{ij} \sin\alpha_{ji} \langle \varepsilon_i^{v'}\, \varepsilon_j^{v'} \rangle \\
\langle \varepsilon_i^{v}\, \varepsilon_j^{v} \rangle &= \sin\alpha_{ij} \sin\alpha_{ji} \langle \varepsilon_i^{u'}\, \varepsilon_j^{u'} \rangle + \cos\alpha_{ij} \cos\alpha_{ji} \langle \varepsilon_i^{v'}\, \varepsilon_j^{v'} \rangle
\end{aligned}\right\} \quad \ldots (2.15)$$

where α_{ij} is the angle between the vector $\mathbf{r}_{ij}$ and the latitude at point i. Thus the final velocity error covariances are

$$\left.\begin{aligned}
\langle \varepsilon_i^{u}\, \varepsilon_j^{u} \rangle &= E_i^{u}\, E_j^{u} \{\cos\alpha_{ij} \cos\alpha_{ji} + \sin\alpha_{ij} \sin\alpha_{ji} (1 - 2a_0 r_{ij}^2)\}\, \mu(\Phi_i, \Phi_j) \\
\langle \varepsilon_i^{u}\, \varepsilon_j^{v} \rangle &= E_i^{u}\, E_j^{u} \{\cos\alpha_{ij} \sin\alpha_{ji} - \sin\alpha_{ij} \cos\alpha_{ji} (1 - 2a_0 r_{ij}^2)\}\, \mu(\Phi_i, \Phi_j) \\
\langle \varepsilon_i^{v}\, \varepsilon_j^{u} \rangle &= E_i^{u}\, E_j^{u} \{\sin\alpha_{ij} \cos\alpha_{ji} - \cos\alpha_{ij} \sin\alpha_{ji} (1 - 2a_0 r_{ij}^2)\}\, \mu(\Phi_i, \Phi_j) \\
\langle \varepsilon_i^{v}\, \varepsilon_j^{v} \rangle &= E_i^{u}\, E_j^{u} \{\sin\alpha_{ij} \sin\alpha_{ji} + \cos\alpha_{ij} \cos\alpha_{ji} (1 - 2a_0 r_{ij}^2)\}\, \mu(\Phi_i, \Phi_j)
\end{aligned}\right\} \quad \ldots (2.16)$$

2.4. *Selection of data for optimal interpolation*

Ideally all data should be used to interpolate to each grid point, this being most important for multivariate analysis when the interpolated increments $(X^a - X^b)$ can be made to obey constraints such as geostrophy and non-divergence in the wind field. Lorenc (1981) has described a scheme which approximates to this ideal, but, in general, computing considerations dictate that some form of selection of the best data must be made for each grid point. This is particularly true in the context of this data assimilation scheme, for otherwise the file of interpolation weights generated for the assimilation stage would be far too large to allow efficient processing.

Data are selected in two stages: firstly the nearest observations falling within a certain radius of influence (5.25° of latitude) are chosen, up to a given maximum number of 30; secondly, for each variable at each level of each grid point, the best data are chosen up to a maximum number of 7. In this context an observation is a reported observation such as an

upper-air ascent which may contain many items of data, e.g. wind, temperature and humidity data at several levels in the vertical.

In the first stage of selection the horizontal distances between the observations and grid points are calculated, and are adjusted by a proportion F of the radius of influence before the search for the nearest is made.

$$\text{adjusted distance} = \text{actual distance} + F \times \text{radius of influence}$$

The factor F is a function of observation type ($F = 0$ for radiosondes, otherwise $F = 1$), and the adjustment is made to ensure that the more valuable multi-level observations, such as upper-air ascents, are selected despite the presence of many nearer single-level observations such as aircraft reports. For each grid point there is also a restriction on the maximum number of observations of a certain type that can be selected. This is to prevent a dense set of observations of a particular type swamping other data types.

In the final stage of selection, the best data are defined as those which, when taken singly, reduce the expected interpolation error E^a by the greatest amount. However, to ensure an even distribution around a grid point, at least one item of data is chosen from each quadrant around the grid point, provided such an item is present. In addition, to maximize the number of independent pieces of information, only one pressure level is selected from each complete observation. These pressure levels (p_i) must be sufficiently close to the grid-point level (p_g). Thus for selection

$$|\ln (p_i/p_g)| < \ln (1.5).$$

2.5. *Quality control*

The quality control of data is performed in two stages. In the first, or Mode 1 check, data are compared to the model background field and any observations differing by more than a critical amount from the expected error are flagged, that is if

$$(X_i^o - X_i^b)^2 > n_1^2 (E_i^{o^2} + E_i^{b^2}). \quad \ldots (2.17)$$

For wind data the vector wind error is checked.

In the second, or Mode 2 check, the observation is compared with a value, X^a, interpolated from surrounding data, and a similar criterion is used to determine whether it should be flagged.

$$(X_i^o - X_i^a)^2 > n_2^2 (E_i^{a^2} + E_i^{o^2}) \quad \ldots (2.18)$$

where n_1 and n_2 are constants used in data checking.

In calculating the interpolated value X^a, neither the observation itself, nor data flagged in Mode 1 or by internal consistency checks, is used. This Mode 2 check is the principal arbiter as to whether data are accepted or rejected, though there is a facility for it to be overruled by the specification of a flag in the initial data sets. Note that although an observation may be flagged in Mode 1, it can still be accepted if it passes the Mode 2 check.

In order to perform both quality-control checks, calculations of the background field values need to be made at observation points. The background field is, in practice, the latest available model forecast valid at the analysis time, and this is a 6-hour forecast from the previous assimilation (or 3 hours in the fine-mesh scheme). Because the model grid has a high

resolution a sufficiently accurate value can be calculated by using bi-linear interpolation in the horizontal and linear in log (pressure) in the vertical. The differences between the observations and these interpolated values can then be calculated, and, with the previously calculated observational and background field errors, the check in expression (2.17) can be made.

Values of n_1 depend on the observation type, those being more liable to gross errors (that is errors which do not belong to the normal error distribution) being assigned smaller values than those less likely to suffer from this defect. An example of the former is an aircraft report, whilst a radiosonde ascent is an example of the latter.

With the observation to be checked taking the place of the grid-point value, equations (2.4) are solved for the interpolation weights W_i by Gaussian elimination and expression (2.18) constructed. The values of n_2 again depend on observation type for the same reasons given for the Mode 1 values. The current specifications for n_1^2 and n_2^2 are given in Table IX.

TABLE IX. *Specifications for n_1^2 and n_2^2*

	Bogus observations	Radiosondes and surface data	Satellite sounding and aircraft reports	Satellite cloud winds
n_1^2	25	12	6	4
n_2^2	25	12	6	4

If more than two levels of a multi-level report are flagged then the entire report is rejected. The non-flagged levels in such a report are regarded with suspicion because they may also be contaminated, though to a lesser extent, by the same feature which caused the other levels to be flagged. Cloud-contaminated satellite temperature soundings are a prime example.

To combat biases in the satellite temperature data, such data are not allowed to participate in the quality control of data from the same source at the Mode 2 stage. This is because nearby data may have a similar bias at one or more levels and incorrect data might easily be reinstated. This is particularly true of high-resolution soundings.

3. ASSIMILATION

3.1. *General description*

In the data assimilation stage the differences of the observations from model values are interpolated to analysis grid points using the optimal interpolation weights calculated as described in the previous section. These differences are then interpolated to the model grid and are used to correct the model at each time-step of a forecast commencing from the previous analysis time and ending at the new analysis time. Figure 4 highlights how the

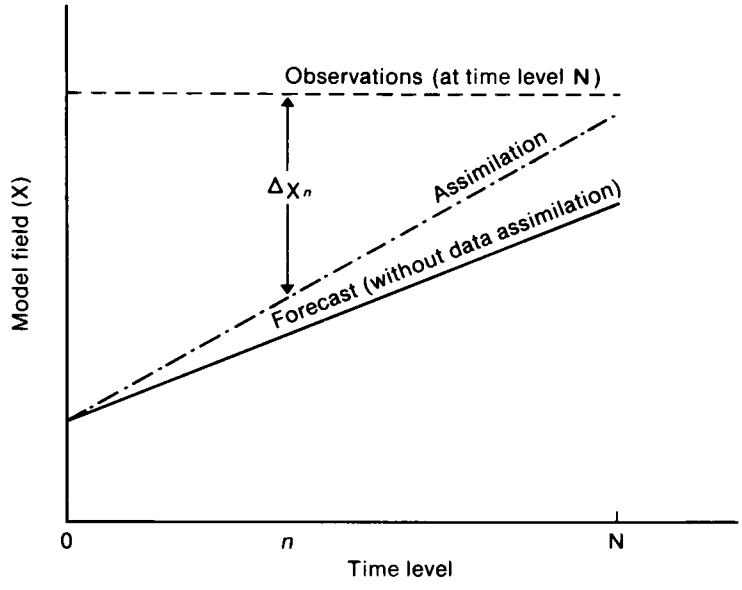

FIGURE 4. Schematic diagram of the assimilation increment

assimilation increment is recalculated each time-step and as the assimilation proceeds the fields adjust towards the observed state. At the end of the period (time N) the assimilated field has approached the observed field but is not identical to it. The fit should, however, be sufficiently close to be within the expected observational errors.

These corrections are scaled by a factor χ and then added into the model fields. Thus a value of $\chi = 0$ corresponds to a model forecast, while $\chi = 1$ for one time-step corresponds to a conventional analysis. An appropriate value of χ can only be adequately determined by experiment and experience since the optimal choice depends on the data available and the scale of the meteorological feature being analysed. Too low a value will lead to a poor fitting of observations, whilst too high a value may excite large amplitude gravity-inertial 'noise'. The technique is analogous to the dynamical relaxation methods of Hoke and Anthes (1976) and Davies and Turner (1977), and is very similar to a form of data assimilation described by Miyakoda *et al.* (1978). Lyne (1979) has analysed the process in a simplified system and has shown that the factor χ can be related to the relaxation coefficient K of Davies and Turner (1977) and Hoke and Anthes (1976) by

$$\chi = K\Delta t/(1 + K\Delta t)$$

where Δt is the time-step of the model. A significant difference from the aforementioned schemes is that the relaxation is towards observed values rather than analysed fields.

The integration scheme of the model is described in more detail in section 5, but for the present it is sufficient to note that it is a split explicit scheme with three adjustment steps to each full advection step. The corrections are calculated once for each advection time-step, scaled by a factor χ and the resulting increments added in at each of the advection time-steps. Further increments based on geostrophic and hydrostatic assumptions are calculated from these corrections in order to hasten the adjustment process during the assimilation.

The assimilation equations can be represented schematically by

$$\left.\begin{aligned} \Delta\mathbf{X} &= \sum_i W_i (X_i^o - X_t) \\ \mathbf{X}'_{t+\Delta t/3} &= \mathrm{A}(\mathbf{X}_t) + \mathrm{D_d}(\mathbf{X}_t) \\ \mathbf{X}'_{t+2\Delta t/3} &= \mathrm{A}(\mathbf{X}'_{t+\Delta t/3}) + \mathrm{D_d}(\mathbf{X}'_{t+\Delta t/3}) \\ \mathbf{X}'_{t+\Delta t} &= \mathrm{A}(\mathbf{X}'_{t+2\Delta t/3}) + \mathrm{D_d}(\mathbf{X}'_{t+2\Delta t/3}) \\ \mathbf{X}_{t+\Delta t} &= \mathrm{B}(\mathbf{X}'_{t+\Delta t}) + \chi\{\Delta\mathbf{X} + \mathrm{H}(\Delta\mathbf{X}) + \mathrm{G}(\Delta\mathbf{X})\} \end{aligned}\right\} \quad \ldots (3.1)$$

where $\mathbf{X}$ is the vector of model fields and $\Delta\mathbf{X}$ are the corrections calculated from the observed values and the model values at time t using the optimal interpolation weights. A prime denotes an intermediate value during the full advection time-step Δt and the operators A and B represent the adjustment and advection terms of the forecast equations respectively. The term B also contains the physical parametrizations. The additional operators H and G represent the hydrostatically derived temperature increments and the geostrophically derived wind increments respectively. Gravity-wave noise generated by local imbalances during the assimilation process could cause initial roughness in the subsequent forecast and this in turn could lead to the rejection of good data in a subsequent quality-control step. This is controlled both by the standard non-linear diffusion of the model (see section 5) and by the addition of a form of divergence damping represented by the operator $\mathrm{D_d}$. These processes are described in more detail in the following subsections.

The final field of assimilation increments are Fourier truncated near the poles to remove unstable modes. Further details of this procedure are described in section 11.

The assimilation of moisture data is rather more complicated than is suggested by equations 3.1. The analysed variable is relative humidity whereas the model variable is specific humidity. First the model moisture field is converted to relative humidity, then the relative humidity increment is added and finally a conversion of the model field back to specific humidity is required.

3.2. *Interpolation to model grid points*

At each full advection time-step the optimum interpolation equation (2.1) is used to calculate corrections at each analysis grid point. The latest available model values are interpolated bi-linearly in the horizontal to observation points, and linearly in log (pressure) in the vertical to the data levels. The difference between observed and model values can then be calculated, and the optimum interpolation weights used to form the assimilation increments at the analysis grid points.

The analysis grid does not coincide with the model grid. To avoid redundant calculations near the poles where Fourier truncation removes unstable modes from the model fields, and to introduce a degree of smoothing into the field of assimilation increments, the analysis grid is quasi-homogeneous poleward of latitudes 50°N and 50°S. In the north–south direction the grid length is the same as the model grid, but in the east–west direction the analysis grid retains approximately the same resolution as at 50° (although the number of grid points per row is not reduced below 16). The variables are not staggered as in the forecast model. In the vertical the analysis grid has the same 15 sigma levels as the model grid. The increments on

the model grid are calculated from those on the analysis grid by bi-linear interpolation in the horizontal.

3.3. *Specification of relaxation coefficients*

Before the increments are added to the model values they are scaled by the relaxation coefficients χ in equation (3.1) which may vary with time and model variable. At the time of writing χ increases linearly in time during the assimilation period from zero to a maximum value of 0.35 at the end of the period for the coarse-mesh model. The maximum value for the fine-mesh model is 0.175. Referring back to Figure 4, it can be seen that the assimilation increment may be relatively large at the start of the assimilation period and it would be undesirable to attempt to apply such large adjustments to the model, hence the use of a small initial value of χ. As the model adjusts towards the observations, the residual increment is smaller, and can be forced in with a greater weight. The value for wind observation increments is reduced during the last few time-steps of the assimilation period to avoid undesirable surface pressure oscillations that would otherwise arise at the start of the subsequent forecast.

3.4. *Geostrophic wind increments*

During the early development of the assimilation scheme it was found that mass data were not always adequately assimilated when there were no supporting wind observations. This could be explained in terms of geostrophic adjustment theory which states that for synoptic scales the mass field tends to adjust to the wind field when they are initially unbalanced (e.g. see Daley 1980). This is a particular problem with surface pressure data. To overcome it geostrophic wind increments are calculated from the assimilation increments of the mass field and, after being suitably scaled, are added to the model wind fields after each advection step. Similar techniques have been employed by other workers, e.g. Kistler and McPherson (1975), Hayden (1973).

The geostrophic equations in σ coordinates are

$$u = \frac{-1}{af}\left(\frac{\partial \Phi}{\partial \phi} + c_p \sigma^\kappa \theta \frac{\partial \Pi}{\partial \phi}\right)$$

$$v = \frac{1}{af\cos\phi}\left(\frac{\partial \Phi}{\partial \lambda} + c_p \sigma^\kappa \theta \frac{\partial \Pi}{\partial \lambda}\right) \qquad \ldots (3.2)$$

where a is the radius of the earth and Π is the Exner function. The geopotential Φ is found by integrating the hydrostatic equation so that at level k

$$\Phi_k = \int_{\sigma_k}^{1} R\Pi\theta\sigma^{(\kappa-1)}\,\mathrm{d}\sigma + \Phi_* \qquad \ldots (3.3)$$

where Φ_* is the geopotential at the surface of the earth.

To calculate geostrophic wind increments the corresponding increment equations can be derived for each level.

$$\left.\begin{aligned}
\Delta u_k &= \frac{-1}{af}\left(\frac{\partial \Delta\Phi_k}{\partial\phi} + c_p\,\sigma_k^\kappa\,\Delta\theta_k\,\frac{\partial\Pi}{\partial\phi} + c_p\,\sigma_k^\kappa\,\theta\,\frac{\partial\Delta\Pi}{\partial\phi}\right)\\
\Delta v_k &= \frac{1}{af\cos\phi}\left(\frac{\partial\Delta\Phi_k}{\partial\lambda} + c_p\,\sigma_k^\kappa\,\Delta\theta_k\,\frac{\partial\Pi}{\partial\lambda} + c_p\,\sigma_k^\kappa\,\theta_k\,\frac{\partial\Delta\Pi}{\partial\lambda}\right)\\
\Delta\Phi_k &= R\int_{\sigma_k}^{1}(\theta_k\,\Delta\Pi + \Pi\Delta\theta_k)\,\sigma^{\kappa-1}\,\mathrm{d}\sigma
\end{aligned}\right\} \quad \ldots (3.4)$$

where terms of $0(\Delta^2)$ have been neglected. The finite difference approximations to these equations are as follows:

$$\left.\begin{aligned}
\Delta u_k &= \frac{-1}{af}\left(\overline{\delta_\phi\,\Delta\Phi_k}^{\lambda} + c_p\,\sigma_k^\kappa\,\overline{\Delta\theta_k}^{\lambda\phi}\,\overline{\delta_\phi\,\Pi}^{\lambda} + c_p\,\sigma_k^\kappa\,\overline{\theta_k}^{\lambda\phi}\,\overline{\delta_\phi\,\Delta\Pi}^{\lambda}\right)\\
\Delta v_k &= \frac{1}{af\cos\phi}\left(\overline{\delta_\lambda\,\Delta\Phi_k}^{\phi} + c_p\,\sigma_k^\kappa\,\overline{\Delta\theta_k}^{\lambda\phi}\,\overline{\delta_\lambda\,\Pi}^{\phi} + c_p\,\sigma_k^\kappa\,\overline{\theta_k}^{\lambda\phi}\,\overline{\delta_\lambda\,\Delta\Pi}^{\phi}\right)\\
\Delta\Phi_k &= R\Delta\Pi\left\{\sum_{m=1}^{k-1}\sigma_m^\kappa\,\theta_m\ln(\sigma_{m-\frac{1}{2}}/\sigma_{m+\frac{1}{2}}) + \sigma_k^\kappa\,\theta_k\ln(\sigma_{k-\frac{1}{2}}/\sigma_k)\right\} +\\
&\quad + R\Pi\left\{\sum_{m=1}^{k-1}\sigma_m^\kappa\,\Delta\theta_m\ln(\sigma_{m-\frac{1}{2}}/\sigma_{m+\frac{1}{2}}) + \sigma_k^\kappa\,\Delta\theta_k\ln(\sigma_{k-\frac{1}{2}}/\sigma_k)\right\}.
\end{aligned}\right\} \quad \ldots (3.5)$$

The operator G in equation (3.1) consists of the above wind increments scaled by a factor (γ_g). This scaling factor has a latitudinal dependence (being 0.25 poleward of latitude 30° and zero equatorward) and a height dependence (being lower at high levels).

3.5. *Hydrostatic temperature increments*

To improve further the fitting of surface pressure data, temperature increments are calculated by a formula derived from the hydrostatic equation. In pressure coordinates equation (3.3) becomes

$$\Phi_k = \int_{p_k}^{p_*} R\theta\left(\frac{p}{1000}\right)^\kappa\frac{\mathrm{d}p}{p} + \Phi_* \quad \ldots (3.6)$$

and with the addition of surface pressure and temperature increments

$$\Phi_k = \int_{p_k}^{p_*+\Delta p_*} R\,(\theta + \Delta\theta)\left(\frac{p}{1000}\right)^\kappa\frac{\mathrm{d}p}{p} + \Phi_*\,. \quad \ldots (3.7)$$

The hydrostatic temperature increments are defined as those which lead to no change in the value of Φ_k when the surface pressure is incremented by Δp_*. Thus from (3.6) and (3.7) we have

$$\int_{p_k}^{p_*+\Delta p_*} R\,(\theta + \Delta\theta)\left(\frac{p}{1000}\right)^\kappa\frac{\mathrm{d}p}{p} = \int_{p_k}^{p_*} R\theta\left(\frac{p}{1000}\right)^\kappa\frac{\mathrm{d}p}{p}\,. \quad \ldots (3.8)$$

If $0(\Delta^2)$ terms are neglected this becomes

$$\frac{\Delta p_*}{p_*} R\theta_* \left(\frac{p_*}{1000}\right)^\kappa = -\int_{p_k}^{p_*} R\Delta\theta \left(\frac{p}{1000}\right)^\kappa \frac{dp}{p}. \quad \ldots (3.9)$$

It is now assumed that $\Delta\theta$ is independent of the pressure p. Then the hydrostatic temperature increments are given by

$$\Delta\theta = -\kappa\,\theta_* \frac{\Delta p_*}{p_*} \frac{\Pi}{\left\{\Pi - \left(\frac{p_k}{1000}\right)^\kappa\right\}}. \quad \ldots (3.10)$$

The lowest level model temperature θ_1 is used in place of the surface temperature θ_*. The operator H in equation (3.1) consists of the above temperature increments scaled by the factor γ_h. It has been found that there is very little correlation between surface pressure changes and temperature changes at the highest model levels and p_k has been set to 225 mb accordingly. The parameter γ_h is 1 for levels below p_k and zero above.

3.6. *Divergence damping*

Because gravity waves generated during the assimilation process generally have larger divergent wind components than meteorological motions, divergence diffusion has been proposed as a method of noise control. Dey (1978) used a modified form which damps only the vertically integrated divergence and hence effectively only the external mode. However, as it was found that this form did not suppress the noise in equatorial regions adequately, the full divergence damping technique has been adopted. By a careful choice of a small value for the damping coefficient K_D (presently 5×10^6 m^2 s^{-1} for the coarse-mesh model) the problems mentioned by Dey when he used the divergence damping at each level have largely been avoided.

The adjustment equations are modified so that

$$\left.\begin{aligned} \frac{\partial u}{\partial t} &= \mathrm{A}_\lambda + \frac{K_D}{a\cos\phi}\frac{\partial D}{\partial \lambda} \\ \frac{\partial v}{\partial t} &= \mathrm{A}_\phi + \frac{K_D}{a}\frac{\partial D}{\partial \phi} \end{aligned}\right\} \quad \ldots (3.11)$$

where D is the divergence, and A_λ and A_ϕ represent the other terms in the equations. The divergence and vorticity equations implied by (3.11) are

$$\left.\begin{aligned} \frac{\partial D}{\partial t} &= \frac{1}{a\cos\phi}\frac{\partial \mathrm{A}_\lambda}{\partial \lambda} + \frac{\partial}{\partial \phi}(\mathrm{A}_\phi \cos\phi) + K_D \nabla^2 D \\ \frac{\partial \zeta}{\partial t} &= \frac{1}{a\cos\phi}\frac{\partial \mathrm{A}_\phi}{\partial \lambda} - \frac{\partial}{\partial \phi}(\mathrm{A}_\lambda \cos\phi) \end{aligned}\right\} \quad \ldots (3.12)$$

where ζ is the vorticity and ∇ is a lateral gradient operator. Hence the divergence diffusion has no effect on vorticity whilst damping the divergence.

The finite difference approximations for the damping terms are as follows:

The divergence D is defined as

$$D = \frac{1}{a\cos\phi}\left\{\frac{\partial u}{\partial\lambda} + \frac{\partial}{\partial\phi}(v\cos\phi)\right\} \quad \ldots (3.13)$$

and its finite difference approximation is

$$D = \frac{1}{a(\cos\phi)}\{\overline{\delta_\lambda u}^{\phi} + \overline{\delta_\phi v(\cos\phi)}^{\lambda}\}. \quad \ldots (3.14)$$

The damping terms in equations (3.11) at each level are then

$$\left.\begin{aligned}\frac{K_D}{a\cos\phi}\frac{\partial D}{\partial\lambda} &= \frac{K_D}{a(\cos\phi)}\overline{\delta_\lambda D}^{\phi}\\ \frac{K_D}{a}\frac{\partial D}{\partial\phi} &= \frac{K_D}{a}\overline{\delta_\phi D}^{\lambda}.\end{aligned}\right\} \quad \ldots (3.15)$$

4. THE FORECAST EQUATIONS

The principal equations which govern motions in the atmosphere are Newton's second law of motion, the first law of thermodynamics, the law of conservation of mass, the equation of state and the conservation equation for water substance.

For large-scale motions of the air, the atmosphere may be assumed to be in hydrostatic equilibrium. In which case, the vertical acceleration may be neglected along with the vertical components of the Coriolis force.

In the (λ, ϕ, σ) coordinate system, the momentum equations may be written as follows:

$$\frac{\partial u}{\partial t} + \frac{u}{a\cos\phi}\frac{\partial u}{\partial\lambda} + \frac{v}{a}\frac{\partial u}{\partial\phi} + \dot\sigma\frac{\partial u}{\partial\sigma} - \left(f + \frac{u\tan\phi}{a}\right)v + \frac{1}{a\cos\phi}\frac{\partial\Phi}{\partial\lambda} + c_p\sigma^\kappa\theta\frac{\partial\Pi}{\partial\lambda} = \mathscr{F}_u \quad \ldots (4.1)$$

$$\frac{\partial v}{\partial t} + \frac{u}{a\cos\phi}\frac{\partial v}{\partial\lambda} + \frac{v}{a}\frac{\partial v}{\partial\phi} + \dot\sigma\frac{\partial v}{\partial\sigma} + \left(f + \frac{u\tan\phi}{a}\right)u + \frac{1}{a}\frac{\partial\Phi}{\partial\phi} + c_p\sigma^\kappa\theta\frac{\partial\Pi}{\partial\phi} = \mathscr{F}_v. \quad \ldots (4.2)$$

The terms $\mathscr{F}_u$ and $\mathscr{F}_v$ represent sources and sinks of momentum due to the sub-grid-scale effects described in sections 6–10, together with dissipation terms.

The thermodynamic equation is

$$\frac{\partial\theta}{\partial t} + \frac{u}{a\cos\phi}\frac{\partial\theta}{\partial\lambda} + \frac{v}{a}\frac{\partial\theta}{\partial\phi} + \dot\sigma\frac{\partial\theta}{\partial\sigma} = \mathscr{F}_\theta \quad \ldots (4.3)$$

and the moisture equation is

$$\frac{\partial q}{\partial t} + \frac{u}{a\cos\phi}\frac{\partial q}{\partial\lambda} + \frac{v}{a}\frac{\partial q}{\partial\phi} + \dot\sigma\frac{\partial q}{\partial\sigma} = \mathscr{F}_q \quad \ldots (4.4)$$

where $\mathscr{F}_\theta$ and $\mathscr{F}_q$ represent sources and sinks of heat and moisture respectively.

The continuity equation in σ coordinates is

$$\frac{\partial p_*}{\partial t} + \frac{1}{a\cos\phi}\frac{\partial}{\partial\lambda}(p_* u) + \frac{\partial}{\partial\phi}(p_* v\cos\phi) + \frac{\partial}{\partial\sigma}(p_*\dot{\sigma}) = 0. \quad \ldots (4.5)$$

The vertical boundary conditions are

$$\dot{\sigma} = 0 \quad \text{at} \quad \sigma = 0, 1. \quad \ldots (4.6)$$

When the continuity equation (4.5) is integrated vertically using these boundary conditions, a predictive equation for the surface pressure is obtained:

$$\frac{\partial p_*}{\partial t} + \frac{1}{a\cos\phi}\int_0^1 \left\{\frac{\partial}{\partial\lambda}(p_* u) + \frac{\partial}{\partial\phi}(p_* v\cos\phi)\right\} d\sigma = 0. \quad \ldots (4.7)$$

The vertical velocity $\dot{\sigma}$ is also given by integrating (4.5):

$$p_*\dot{\sigma} = -\frac{1}{a\cos\phi}\int_0^\sigma \left\{\frac{\partial}{\partial\lambda}(p_* u) + \frac{\partial}{\partial\phi}(p_* v\cos\phi)\right\} d\sigma - \sigma\frac{\partial p_*}{\partial t}. \quad \ldots (4.8)$$

The geopotential Φ is determined from the hydrostatic equation:

$$\frac{\partial\Phi}{\partial\sigma} + \frac{RT_v}{\sigma} = 0 \quad \ldots (4.9)$$

where T_v is virtual temperature, given by $T_v = T(1 + 0.61q)$, and T is related to θ by

$$T = \theta\left(\frac{p}{1000}\right)^\kappa. \quad \ldots (4.10)$$

5. THE INTEGRATION SCHEME

The model uses a split explicit integration scheme similar to that introduced by Gadd (1978a). The equations are split into two parts, called the 'adjustment' and 'advection' steps. The former includes the pressure gradient and Coriolis terms as well as the terms which involve the vertical velocity, $\dot{\sigma}$, and the latter consists of the horizontal advection terms together with the lateral diffusion terms. The effects of the sub-grid-scale parametrizations are added in during the advection stage. Each complete time-step of length Δt (15 minutes in the global model) consists of three adjustment steps of length $\delta t = \Delta t/3$, followed by an advection step of length Δt which is carried out by a two-step Lax–Wendroff method.

In the following description superscript n indicates the time level and we use the standard finite-difference notation:

$$\delta_x A = \{A(x + \tfrac{1}{2}\Delta x) - A(x - \tfrac{1}{2}\Delta x)\}/\Delta x$$
$$\overline{A}^x = \{A(x + \tfrac{1}{2}\Delta x) + A(x - \tfrac{1}{2}\Delta x)\}/2.$$

5.1. *The adjustment step*

The adjustment step uses a 'forward–backward' scheme in which a forward difference in

time is used for the p_*, q, and θ equations, and the new values of these variables are then used in the u and v equations. The 'forward' part of the integration scheme is:

$$p_*^{n+1} = p_*^n - \frac{\delta t}{a\cos\phi}\left\{\delta_\lambda\left(\overline{\bar{p}_*^{\lambda\phi}\sum_{m=1}^{\mathrm{TOP}} u_m\,\Delta\sigma_m}^{\phi}\right) + \right.$$

$$\left. + \delta\phi\left(\overline{\cos\phi\,\bar{p}_*^{\lambda\phi}\sum_{m=1}^{\mathrm{TOP}} v_m\,\Delta\sigma_m}^{\lambda}\right)\right\}^n \qquad \ldots (5.1)$$

$$\theta^{n+1} = \theta^n - \delta t\left(\dot\sigma\frac{\partial\theta}{\partial\sigma}\right)^n \qquad \ldots (5.2)$$

$$q^{n+1} = q^n - \delta t\left(\dot\sigma\frac{\partial q}{\partial\sigma}\right)^n. \qquad \ldots (5.3)$$

The finite-difference form chosen for the vertical advection terms in (5.2) and (5.3) conserves the heat and moisture content of a vertical column. For potential temperature advection.

$$\dot\sigma\frac{\partial\theta}{\partial\sigma} = \overline{\dot\sigma\delta_\sigma\theta}^{\sigma} = \frac{1}{2\Delta\sigma_k}\{(\theta_k - \theta_{k-1})\,\dot\sigma^{k-\frac12} + (\theta_{k+1} - \theta_k)\,\dot\sigma^{k+\frac12}\} \qquad \ldots (5.4)$$

in (5.2) with a similar expression in (5.3).

The vertical velocity $\dot\sigma$ is given by

$$(p_*\,\dot\sigma)_{k+\frac12} = \frac{-1}{a\cos\phi}\left(\sum_{m=1}^{k} - \sigma_{k+\frac12}\sum_{m=1}^{\mathrm{TOP}}\right)\{\overline{\delta_\lambda(\bar{p}_*^{\lambda\phi}u)}^{\phi} + \overline{\delta\phi(\cos\phi\,\bar{p}_*^{\lambda\phi}v)}^{\lambda}\}_m\,\Delta\sigma_m. \qquad \ldots (5.5)$$

The 'backward' part of the integration scheme is given by

$$u^{n+1} = u^n + \delta t\,[\tfrac12 F^n(v^n + v^{n+1}) - \overline{\dot\sigma^{n\lambda\phi}\delta_\sigma u^n}^{\sigma} -$$

$$- \frac{1}{a\cos\phi}\overline{\{\delta_\lambda\Phi^{n+1} + c_p\sigma^\kappa(\bar\theta^\lambda\delta_\lambda\Pi)^{n+1}\}}^{\phi}] \qquad \ldots (5.6)$$

$$v^{n+1} = v^n - \delta t\,[\tfrac12 F^n(u^n + u^{n+1}) + \overline{\dot\sigma^{n\lambda\phi}\delta_\sigma v^n}^{\sigma} +$$

$$+ \frac{1}{a}\overline{\{\delta_\phi\Phi^{n+1} + c_p\sigma^\kappa(\bar\theta^\phi\delta_\phi\Pi)^{n+1}\}}^{\lambda}] \qquad \ldots (5.7)$$

where $F^n = (f + u^n\tan\phi/a)$.

Note that the vertical advection terms in equations (5.2), (5.3), (5.6) and (5.7) are integrated with a forward time-step, which is numerically unstable. In practice, however, this tendency is compensated for by damping elsewhere in the model.

The Coriolis terms in equations (5.6) and (5.7) are handled by a centred implicit step in order to eliminate a source of instability noted by Gadd (1980); this is essential for

integrations of more than a few days. The scheme remains explicit, however, since equations (5.6) and (5.7) may be rearranged to give

$$u^{n+1} = W_1 u^n + W_2 v^n - W_3 \dot{\sigma} \frac{\partial u^n}{\partial \sigma} - W_4 \dot{\sigma} \frac{\partial v^n}{\partial \sigma} - W_3 P_\lambda^n - W_4 P_\phi^n$$

$$v^{n+1} = W_1 v^n + W_2 u^n - W_3 \dot{\sigma} \frac{\partial v^n}{\partial \sigma} + W_4 \dot{\sigma} \frac{\partial u^n}{\partial \sigma} - W_3 P_\phi^n - W_4 P_\lambda^n$$

where

$$W_1 = (1 - F^2 \delta t^2/4)/(1 + F^2 \delta t^2/4), \qquad W_2 = F\delta t/(1 + F^2 \delta t^2/4),$$
$$W_3 = \delta t/(1 + F^2 \delta t^2/4), \qquad W_4 = (F\delta t^2/2)/(1 + F^2 \delta t^2/4),$$
$$P_\lambda = \frac{1}{a \cos\phi} \frac{\partial \Phi}{\partial \lambda} + c_p \sigma^\kappa \theta \frac{\partial \Pi}{\partial \lambda} \quad \text{and} \quad P_\phi = \frac{1}{a} \frac{\partial \Phi}{\partial \phi} + c_p \sigma^\kappa \theta \frac{\partial \Pi}{\partial \phi}.$$

The geopotential Φ required in equations (5.6) and (5.7) is computed by the following discrete form of the hydrostatic equation:

$$\Phi_k = \Phi_* + \sum_{m=1}^{k-1} R(T_v)_m \ln\left(\frac{\sigma_{m-\frac{1}{2}}}{\sigma_{m+\frac{1}{2}}}\right) + R(T_v)_k \ln\left(\frac{\sigma_{k-\frac{1}{2}}}{\sigma_k}\right). \qquad \ldots (5.8)$$

5.2. *Grid splitting*

The finite-difference scheme described above suffers from grid separation, since the 'B' grid supports two independent solutions for gravity waves. This decoupling can be forced by the boundary conditions and experience has shown that its effects are more apparent in limited-area versions of the model. To prevent it, a scheme devised by Mesinger (1973) and extended by Janjic (1979) is used. It is applied in slightly different forms in the fine-mesh and coarse-mesh versions of the model.

A term of the form

$$w\delta t^2 \sum_{m=1}^{\text{TOP}} (\nabla_+^2 - \nabla_\times^2) P_m \Delta\sigma_m$$

is added to the right-hand side of equation (5.1) in all versions of the model, where

$$\nabla_+^2 P_k = \frac{1}{a^2 \cos^2\phi} \{\delta_\lambda (\bar{p}_*^{\lambda} \delta_\lambda \Phi) + \delta_\lambda (c_p \bar{\theta}^{\lambda} \sigma^\kappa \bar{p}_*^{\lambda} \delta_\lambda \Pi)\} +$$
$$+ \frac{1}{a^2 \cos\phi} \{\delta_\phi (\cos\phi \bar{p}_*^{\phi} \delta_\phi \Phi) + \delta_\phi (\cos\phi c_p \bar{\theta}^{\phi} \sigma^\kappa \bar{p}_*^{\phi} \delta_\phi \Pi)\} \qquad \ldots (5.9)$$

$$\nabla_\times^2 P_k = \frac{1}{a^2 \cos^2\phi} \{\delta_\lambda (\overline{\bar{p}_*^{\lambda\phi}}^{\phi} \delta_\lambda \Phi) + \delta_\lambda (c_p \overline{\bar{p}_*^{\lambda\phi}}^{\phi} \sigma^\kappa \overline{\bar{\theta}^{\lambda}}^{\phi} \delta_\lambda \Pi)\} +$$
$$+ \frac{1}{a^2 \cos\phi} \{\delta_\phi (\cos\phi \overline{\bar{p}_*^{\lambda\phi}}^{\lambda} \delta_\phi \Phi) + \delta_\phi (\cos\phi c_p \overline{\bar{p}_*^{\lambda\phi}}^{\lambda} \sigma^\kappa \overline{\bar{\theta}^{\phi}}^{\lambda} \delta_\phi \Pi)\}. \qquad \ldots (5.10)$$

This prevents grid splitting in treating the external gravity waves, ensuring that perturbations in the height field are immediately felt at all the surrounding grid points.

In the fine-mesh model, grid separation for all the internal gravity waves is prevented in a similar fashion, a term of the form

$$w\,\delta t^2 \sum_{m=1}^{k} (\nabla_+^2 - \nabla_\times^2)\, P_m\, \Delta\sigma_m$$

being added to the right-hand side of equation (5.5).

An upper limit for the value of the parameter w may be inferred from linear stability theory. The maximum allowed for stability is $w = 0.25$. At present a value of $w = 0.125$ is used in the fine-mesh version of the model and $w = 0.0625$ in the coarse-mesh.

5.3. *The advection step*

The two-step Lax–Wendroff integration scheme for the advection step uses the modification due to Gadd (1978b, 1980), which reduces phase and amplitude errors. The scheme is 'time-staggered' with the variables (θ, q) and (u, v) changing places at the end of the first step. The finite-difference equations for the first step are:

$$\theta^{n+\frac{1}{2}} = \left[\bar{\theta}^{\lambda\phi} - \Delta t \left\{ \left(\frac{u}{a\cos\phi} \right) \delta_\lambda \bar{\theta}^{\phi} + \frac{v}{a} \delta_\phi \bar{\theta}^{\lambda} \right\} \right]^n \qquad \ldots (5.11)$$

$$q^{n+\frac{1}{2}} = \left[\bar{q}^{\lambda\phi} - \Delta t \left\{ \left(\frac{u}{a\cos\phi} \right) \delta_\lambda \bar{q}^{\phi} + \frac{v}{a} \delta_\phi \bar{q}^{\lambda} \right\} \right]^n \qquad \ldots (5.12)$$

$$u^{n+\frac{1}{2}} = \left[\bar{u}^{\lambda\phi} - \Delta t \left\{ \left(\frac{\bar{u}^{\lambda\phi}}{a\cos\phi} \right) \delta_\lambda \bar{u}^{\phi} + \frac{\bar{v}^{\lambda\phi}}{a} \delta_\phi \bar{u}^{\lambda} \right\} \right]^n \qquad \ldots (5.13)$$

$$v^{n+\frac{1}{2}} = \left[\bar{v}^{\lambda\phi} - \Delta t \left\{ \left(\frac{\bar{u}^{\lambda\phi}}{a\cos\phi} \right) \delta_\lambda \bar{v}^{\phi} + \frac{\bar{v}^{\lambda\phi}}{a} \delta_\phi \bar{v}^{\lambda} \right\} \right]^n. \qquad \ldots (5.14)$$

In the second step we use fourth-order approximations to the derivatives:

$$\theta^{n+1} = \theta^n - \Delta t \left[\frac{u}{a\cos\phi} \{(1 + c)\,\delta_\lambda \bar{\theta}^{\phi} - c(\tfrac{2}{3}\delta_{3\lambda} \bar{\theta}^{\phi} + \tfrac{1}{3}\delta_{3\lambda} \bar{\theta}^{3\phi})\} + \right.$$
$$\left. + \frac{v}{a} \{(1 + c)\,\delta_\phi \bar{\theta}^{\lambda} - c(\tfrac{2}{3}\delta_{3\phi} \bar{\theta}^{\lambda} + \tfrac{1}{3}\delta_{3\phi} \bar{\theta}^{3\lambda})\} \right]^{n+\frac{1}{2}} \qquad \ldots (5.15)$$

$$q^{n+1} = q^n - \Delta t \left[\frac{u}{a\cos\phi} \{(1 + c)\,\delta_\lambda \bar{q}^{\phi} - c(\tfrac{2}{3}\delta_{3\lambda} \bar{q}^{\phi} + \tfrac{1}{3}\delta_{3\lambda} \bar{q}^{3\phi})\} + \right.$$
$$\left. + \frac{v}{a} \{(1 + c)\,\delta_\phi \bar{q}^{\lambda} - c(\tfrac{2}{3}\delta_{3\phi} \bar{q}^{\lambda} + \tfrac{1}{3}\delta_{3\phi} \bar{q}^{3\lambda})\} \right]^{n+\frac{1}{2}} \qquad \ldots (5.16)$$

$$u^{n+1} = u^n - \Delta t \left[\frac{\bar{u}^{\lambda\phi}}{a\cos\phi} \{(1 + c)\,\delta_\lambda \bar{u}^{\phi} - c(\tfrac{2}{3}\delta_{3\lambda} \bar{u}^{\phi} + \tfrac{1}{3}\delta_{3\lambda} \bar{u}^{3\phi})\} + \right.$$
$$\left. + \frac{\bar{v}^{\lambda\phi}}{a} \{(1 + c)\,\delta_\phi \bar{u}^{\lambda} - c(\tfrac{2}{3}\delta_{3\phi} \bar{u}^{\lambda} + \tfrac{1}{3}\delta_{3\phi} \bar{u}^{3\lambda})\} \right]^{n+\frac{1}{2}} \qquad \ldots (5.17)$$

$$v^{n+1} = v^n - \Delta t \left[\frac{\bar{u}^{\lambda\phi}}{a\cos\phi} \{(1 + c)\,\delta_\lambda \bar{v}^{\phi} - c(\tfrac{2}{3}\delta_{3\lambda}\bar{v}^{\phi} + \tfrac{1}{3}\delta_{3\lambda}\bar{v}^{3\phi})\} + \right.$$
$$\left. + \frac{\bar{v}^{\lambda\phi}}{a} \{(1 + c)\delta_\phi \bar{v}^{\lambda} - c(\tfrac{2}{3}\delta_{3\phi}\bar{v}^{\lambda} + \tfrac{1}{3}\delta_{3\phi}\bar{v}^{3\lambda})\} \right]^{n+\frac{1}{2}}. \quad \ldots \quad (5.18)$$

In equations (5.15)–(5.18), the parameter c is given by $c = \frac{3}{4}(1 - \mu^2)$ where μ is the Courant number,

$$\mu = \left(\frac{u^2\Delta t^2}{a^2\cos^2\phi\Delta\lambda^2} + \frac{v^2\Delta t^2}{a^2\Delta\phi^2} \right)^{\frac{1}{2}}. \quad \ldots \quad (5.19)$$

The above value of c is the one which leads to the smallest amount of damping by the advection scheme. Other values of c may be chosen, for example that which minimizes the phase errors (Carpenter 1981).

5.4. *Horizontal diffusion*

Small-scale high-frequency noise can develop during a forecast as a result of the energy cascade down to smaller scales. A dissipation term is used to suppress this noise and keep the model fields smooth.

The changes during a time-step due to horizontal diffusion are calculated at time level n and added to the right-hand side of equations (5.15)–(5.18). Non-linear diffusion of the form $K\,|\nabla^2 X|\,\nabla^2 X$ is used, this being more scale selective than linear diffusion. In finite-difference form

$$\nabla^2 X = \frac{1}{a^2\cos^2\phi}\,\delta_{\lambda\lambda} X + \frac{1}{a^2\cos\phi}\,\delta_\phi(\cos\phi\,\delta_\phi X) \quad \ldots \quad (5.20)$$

where $X = (\theta, q, u \text{ or } v)$. The diffusion coefficient K is chosen to give the minimum necessary damping. In global forecasts $K = 2 \times 10^{14}\ \mathrm{m^4\,s^{-1}}$ for θ, u and v, and $K = 2 \times 10^{17}\ \mathrm{m^4\,s^{-1}}$ for q. Higher-resolution forecasts use smaller values of K that are consistent with the change in grid length and time-step.

5.5. *Vertical diffusion*

Small-scale noise can also occasionally develop in the vertical especially in the wind field at upper levels in low latitudes. Vertical diffusion is therefore applied above 600 mb and takes the form

$$\frac{\partial \mathbf{v}}{\partial t} = K \frac{(\cos\phi - \cos\hat{\phi})}{(1 - \cos\hat{\phi})} \frac{\partial^2 \mathbf{v}}{\partial\sigma^2} \quad \ldots \quad (5.22)$$

where $K = 10^{-8}\ \mathrm{s^{-1}}$ and $\hat{\phi} = 30°$. The effective diffusion therefore tails off away from the equator and is taken to be zero for $\phi > \hat{\phi}$.

6. DYNAMIC PRECIPITATION

Large-scale or dynamic precipitation is produced when the air at model grid points becomes supersaturated as a result of ascent or radiative cooling. The parametrization scheme removes this excess moisture and allows it to fall as rain or snow. The effects of evaporation and the melting of snow on the falling precipitation are also taken into account.

6.1. *The formation of precipitation through condensation*

Starting at the top of the model, the following calculation is performed for each level k in turn. First, the specific humidity, q_k, is compared with the saturation specific humidity $q_s(T_k)$, corresponding to the temperature T_k at that grid point. If $q_k \leqslant q_s(T_k)$, and there is no precipitation falling from higher levels, then we proceed to the next level below.

If $q_k > q_s(T_k)$, then the excess moisture is removed and the temperature is increased through the release of latent heat. Defining adjusted values of q_k and T_k by $q_s(T'_k)$ and $T'_k = (T_k + \Delta T_k)$, we have

$$\Delta T_k = \frac{L_c}{c_p}\{q_k - q_s(T'_k)\}, \qquad \ldots (6.1)$$

where L_c is the latent heat of condensation. The adjustment is made so that the grid point is just saturated at the new temperature. On using the Clausius–Clapeyron relation, we have

$$q_s(T'_k) = q_s(T_k) + \frac{\partial q_s}{\partial T}(T_k)\,\Delta T_k = q_s(T_k)\left(1 + \frac{\varepsilon L_c\,\Delta T_k}{RT_k^2}\right) \qquad \ldots (6.2)$$

where ε is the ratio of the molecular weights of water and dry air. Equations (6.1) and (6.2) can be solved simultaneously for ΔT_k and $q_s(T'_k)$, the new value of $q_s(T'_k)$ being given by

$$q_s(T'_k) = q'_k = q_k - \frac{\{q_k - q_s(T_k)\}}{\{1 + \varepsilon L_c^2\, q_s(T_k)/(c_p RT_k^2)\}}. \qquad \ldots (6.3)$$

If $T_k < 273$ K, the precipitation formed is assumed to freeze. A further contribution to the temperature increment is then derived from the additional latent heat released.

The precipitation per unit mass, P, at level k resulting from the calculation at this level, given by

$$P_k = q_k - q_s(T'_k), \qquad \ldots (6.4)$$

is added to any precipitation reaching this level from above.

6.2. *Evaporation*

If $q_k < q_s(T'_k)$, that is the air is not saturated at level k, and precipitation is falling from higher levels, a proportion is evaporated. The evaporation formula is designed to give evaporation rates which are typically of the order of 7 mm/day/100 mb. The evaporation per unit mass, E, at level k is given by

$$E_k = \min\left[\beta\{q_s(T_k) - q_k\}\,\Delta t,\ P_k\right] \qquad \ldots (6.5)$$

where $\beta = 2 \times 10^{-5} s^{-1}$, Δt is the time-step and P_k is the precipitation falling through the layer.

New values of q_k and T_k, say q_k'' and T_k'', as a result of the above evaporation are given by

$$q_k'' = q_k + E_k \quad \text{and} \quad T_k'' = T_k - L_c E_k / c_p.$$

If the precipitation is frozen, the latent heat of sublimation is used in place of L_c.

6.3. *The melting of snow*

Snow is melted in the highest model layer whose temperature is greater than 273 K. All the precipitation falling into this layer is assumed to melt immediately. The accompanying change in temperature is therefore given by

$$\Delta T_k = -\frac{L_f}{c_p} \sum_{m=k+1}^{\text{TOP}} (P_m - E_m) \qquad \ldots (6.6)$$

where L_f is the latent heat of fusion.

A similar adjustment is made to the temperature field if the precipitation changes from rain to snow.

6.4. *The precipitation reaching the surface*

From the above the amount of dynamic precipitation reaching the surface in one time-step, A_*, may be calculated. Expressed in millimetres per unit area

$$A_* = \frac{10^2}{g} p_* \sum_{m=1}^{\text{TOP}} (P_m - E_m)\, \Delta\sigma_m \qquad \ldots (6.7)$$

The rate of precipitation, W_*, in millimetres per hour is then given by

$$W_* = (3600/\Delta t)\, A_*. \qquad \ldots (6.8)$$

7. DEEP CONVECTION

The deep convection scheme, originally described by Lyne and Rowntree (1976), was developed using data from the Global Atmospheric Research Programme Atlantic Tropical Experiment. It is based on parcel theory modified by entrainment (Riehl 1954, Scorer 1958, Ludlam 1963) with a treatment of detrainment based on Ceselski (1972) and Arakawa (1969).

The formulation contains a number of parameters whose values have to be determined by experiment. Their values have therefore been modified in the light of experience from the values originally quoted by Lyne and Rowntree. Those in current use are shown in Table X. An overview of the logic of the scheme can be obtained from the flow diagram given in Figure 5. Details of the modelling of the fluxes between the cloud and the environment and also adjacent levels are given in Figure 6.

The bottom two levels of the operational model are combined for the purpose of

TABLE X. *Values of adjustable parameters used in the deep convection scheme*

Parameter	Meaning	Value
b	Excess buoyancy of parcel for continuance of convection	0.2 K
$\varepsilon_{k+\frac{1}{4}}$	Fractional entrainment rate at level $k + \frac{1}{4}$	$3A_E\sigma_k(\sigma_k - \sigma_{k+\frac{1}{2}})$
$\varepsilon_{k+\frac{3}{4}}$	Fractional entrainment rate at level $k + \frac{3}{4}$	$3A_E\sigma_{k+\frac{1}{2}}(\sigma_{k+\frac{1}{2}} - \sigma_{k+1})$
c, d	Constants in initial mass flux formula	10^{-3} K^{-1}, 0.0
M_{MIN}	Minimum mass flux	$10^{-3} c E_{MIN}$
s_θ, s_q	Excess of initial parcel values over the environment	0.2 K, 0.0 kg kg^{-1}
E_{MIN}	Minimum parcel buoyancy	1 K
A_E	Entrainment factor	1.0 $k = 1$ 1.5 $k > 1$
η_k	Fractional mixing detrainment rate at level k	$(\varepsilon_{k+\frac{1}{4}} + \varepsilon_{k+\frac{3}{4}})(1 - A_E^{-1})$

convection, since parcel theory is not appropriate near the earth's surface. A dry convective adjustment step is performed as part of the boundary-layer calculations to represent the effect of the well-mixed layer in unstable conditions.

7.1. *The buoyancy equations*

The scheme assumes that in each grid box there is an ensemble of buoyant convective plumes with varying characteristics (temperature, humidity, cross-sectional area) which entrain air from the surrounding environment and ascend until they are no longer buoyant. Within the ensemble the virtual potential temperatures of the plumes θ_v^P, are further assumed to be distributed about an average value

$$(\theta_v^P)_k = \theta_k^P (1 + 0.61\, q_k^P). \qquad \ldots (7.1)$$

Here q_k^P is the average specific humidity of the plumes at level k with $q_k^P \leqslant q_s(\theta_k^P)$.

The finite difference treatment of the ensemble is best understood by reference to Figure 6. We define δ_k as the fractional rate of forced detrainment at level k, η_k as the fractional rate of detrainment due to mixing and $\varepsilon_{k+\frac{1}{4}}, \varepsilon_{k+\frac{3}{4}}$ as the fractional entrainment rates at levels $k + \frac{1}{4}$, $k + \frac{3}{4}$. The entrainment and mixing detrainment rates are specified empirically (see Table X), whilst the forced detrainment rate is diagnosed by the convection scheme. Forced detrainment occurs at those levels where it is necessary to maintain buoyancy and may be interpreted as the fraction of the ensemble whose plumes terminate at that level. The effects of entrainment and mixing detrainment, on the other hand, are assumed to act at all levels and represent the mixing processes near the edges of updraughts which transfer air both into and out of a plume.

The vertical mass flux M at level k, gives a measure of the size of the ensemble and is predicted by

$$M_{k+1} = (1 + \varepsilon_{k+\frac{1}{4}})(1 + \varepsilon_{k+\frac{3}{4}})(1 - \delta_k)(1 - \eta_k) M_k. \qquad \ldots (7.2)$$

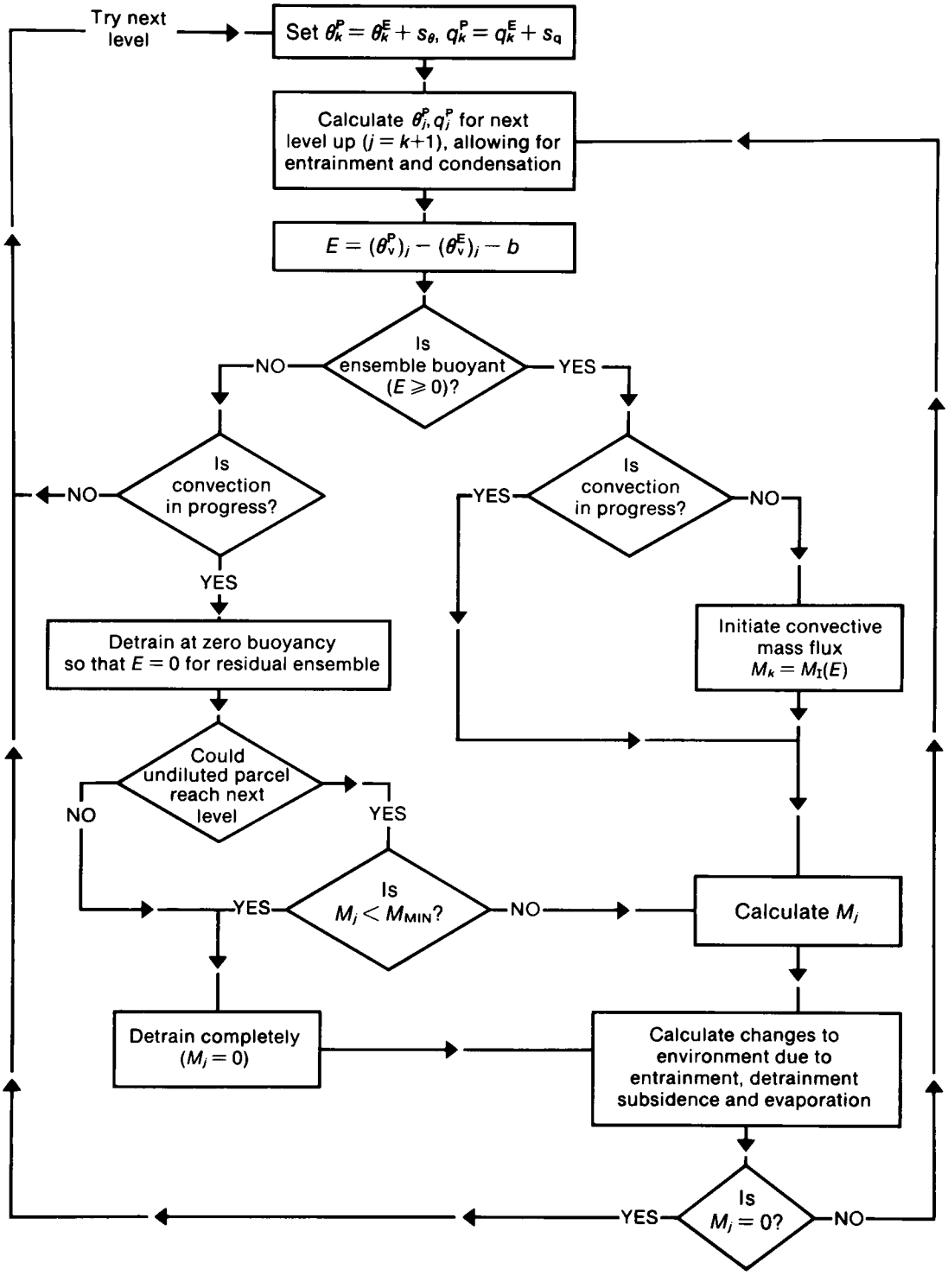

FIGURE 5. Flow diagram of the structure of the convection scheme. See text for explanation of symbols.

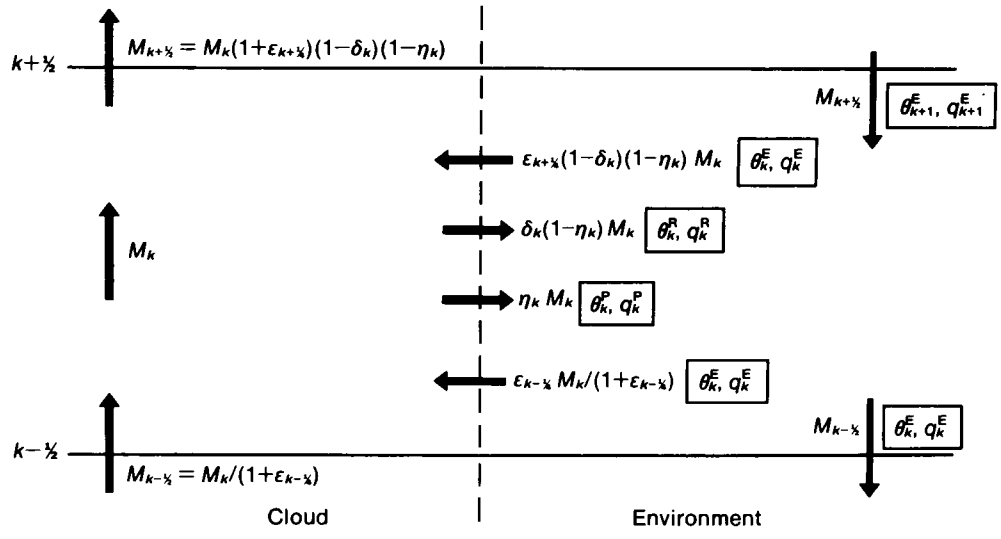

FIGURE 6. Vertical fluxes, entrainment and detrainment in the convection scheme

The treatment of the ensemble as it passes from level k to level $k + 1$ is independent of η_k and is described by the following equations:

$$(1 + \varepsilon_{k+\frac{1}{2}})(1 + \varepsilon_{k+\frac{1}{2}})(1 - \delta_k)\, q^{\mathrm{P}}_{k+1} = q^{\mathrm{P}}_k - \delta_k q^{\mathrm{R}}_k + \varepsilon_{k+\frac{1}{2}}(1 - \delta_k)\, q^{\mathrm{E}}_k + \varepsilon_{k+\frac{1}{2}}(1 + \varepsilon_{k+\frac{1}{2}})(1 - \delta_k)\, q^{\mathrm{E}}_{k+1} \quad \ldots (7.3)$$

$$(1 + \varepsilon_{k+\frac{1}{2}})(1 + \varepsilon_{k+\frac{1}{2}})(1 - \delta_k)\left[\theta^{\mathrm{P}}_{k+1} - \frac{L_c}{c_p}\gamma_{k+1}\left\{q^{\mathrm{P}}_{k+1} - q_s(\theta^{\mathrm{P}}_{k+1})\right\}\sigma^{-\kappa}_{k+1}\,\Pi^{-1}\right] = \theta^{\mathrm{P}}_k - \delta_k\theta^{\mathrm{R}}_k + \varepsilon_{k+\frac{1}{2}}(1 - \delta_k)\,\theta^{\mathrm{E}}_k + \varepsilon_{k+\frac{1}{2}}(1 + \varepsilon_{k+\frac{1}{2}})(1 - \delta_k)\,\theta^{\mathrm{E}}_{k+1} \quad \ldots (7.4)$$

where q^{P}_k is the specific humidity of the ensemble before the condensation and $\gamma_k = 1$ if $q^{\mathrm{P}}_k \geqslant q_s(\theta^{\mathrm{P}}_k)$; otherwise $\gamma_k = 0$. A superscript E refers to environmental values whilst a superscript R refers to detrainment values. The latent heat of condensation is either with respect to water or to ice depending on temperature.

7.2. *Forced detrainment*

Forced detrainment does not take place at the lowest convective level. Indeed at higher levels this process only takes place when it is necessary to make the ensemble buoyant at the next level.

The ensemble is first raised from level k to level $k + 1$ without the effects of forced detrainment. This is done by solving equations (7.3) and (7.4) with $\delta_k = 0$. The Clausius–Clapeyron relation is used to approximate $q_s(\theta^{\mathrm{P}}_{k+1})$ in equation (7.4) by

$$q_s(\theta^{\mathrm{P}}_{k+1}) = q_s(\theta^{\mathrm{E}}_{k+1})\left\{1 + \frac{L_c}{R_v}\frac{(\theta^{\mathrm{P}}_{k+1} - \theta^{\mathrm{E}}_{k+1})}{(T^{\mathrm{E}}_{k+1})^2}(\sigma_{k+1})^{\kappa}\,\Pi\right\} \quad \ldots (7.5)$$

where R_v is the gas constant for water vapour.

If it is found that the virtual potential temperature of the ensemble is greater by a quantity b than that of the environmental air, that is

$$(\theta_v^P)_{k+1} - b > (\theta_v^E)_{k+1} \quad \ldots (7.6)$$

then the ensemble is assumed to be buoyant at this level and no forced detrainment occurs. The minimum excess buoyancy b allows for the spread of θ_v^P in the ensemble. Thus the characteristics of the ensemble at level k are now known.

If equation (7.6) is not initially satisfied, then sufficient detrainment is allowed to occur at level k at a virtual potential temperature of θ_v^E so that (7.6) becomes satisfied. Therefore, defining the virtual potential temperature of detraining air by

$$(\theta_v^R)_k = \theta_k^R \{1 + 0.61\,\gamma_k q_s(\theta_k^R) + 0.61\,(1 - \gamma_k)\,q_k^P\} \quad \ldots (7.7)$$

we can set

$$(\theta_v^R)_k = (\theta_v^E)_k. \quad \ldots (7.8)$$

The potential temperature of detraining air may now be derived from equations (7.7) and (7.8) by using the Clausius–Clapeyron relationship (see equation (7.5)) with the approximation

$$\theta_k^R\, q_s(\theta_k^R) = \theta_k^E\, q_s(\theta_k^R)$$

whence

$$\theta_k^R = \theta_k^E \left[1 + \frac{0.61\,\{q_k^E - q_s(\theta_k^E)\}}{1 + 0.61\,L_c/(R_v\,T_k^E)\,q_s(\theta_k^E)} \right]. \quad \ldots (7.9)$$

The forced detrainment rate δ_k may now be determined from equations (7.3) and (7.4) together with equation (7.9) by choosing a value for θ_{k+1}^P such that the ensemble is just buoyant; the buoyancy test (7.6) is treated in the same way as the derivation of equation (7.9) to give

$$\theta_{k+1}^P = \theta_{k+1}^E + \frac{0.61\,\theta_{k+1}^E\,\{q_{k+1}^E - q_s(\theta_{k+1}^E)\} + b}{1 + 0.61\,L_c/(R_v\,T_{k+1}^E)\,q_s(\theta_{k+1}^E)}. \quad \ldots (7.10)$$

When dry convection is necessary, that is $\gamma_k = \gamma_{k-1} = 0$, this reduces to

$$\theta_{k+1}^P = \frac{\theta_{k+1}^E\,(1 + 0.61\,q_{k+1}^E) + b}{1 + 0.61\,q_{k+1}^P}. \quad \ldots (7.11)$$

7.3. *Initiation of convection*

The model atmosphere is tested from the bottom upwards for convective instability by taking a parcel from level k to level $k + 1$ with

$$\theta_k^P = \theta_k^E + s_\theta \text{ and } q_k^P = q_k^E + s_q$$

where s_θ and s_q are constants (see Table X). Convection is then initiated if the buoyancy test

$$(\theta_v^P)_{k+1} - (\theta_v^E)_{k+1} - b \geqslant E_{MIN}\,\Delta\sigma_{k+\frac{1}{2}} \qquad \ldots (7.12)$$

is satisfied. Here E_{MIN} is a constant and represents the minimum buoyancy required by the ensemble for convection to begin.

The initial mass flux, M_I, ascribed to the ensemble is based on the excess buoyancy occurring in a time-step and is given by

$$M_I = 10^{-3}\left\{d + c\,\frac{(\theta_v^P)_{k+1} - (\theta_v^E)_{k+1} - b}{\Delta\sigma_{k+\frac{1}{2}}}\right\}. \qquad \ldots (7.13)$$

Here d and c are constants (see Table X). The parameter d is designed to allow some convection to take place independently of the amount of excess buoyancy. M_I is additionally constrained to be smaller than the depth of the thinnest model layer to prevent over-stabilization.

7.4. *Termination of convection*

Convection continues upwards through the model atmosphere until the ensemble is no longer buoyant. This occurs when the upward mass flux becomes so small (less than a critical mass flux M_{MIN}) that the effects of convection would be negligible. Convection is therefore terminated when the residual mass flux

$$(1 - \eta_k)(1 - \delta_k)M_k < M_{MIN} \qquad \ldots (7.14)$$

with detrainment taking place at level k using the parcel values q_k^P and θ_k^P.

Convection is also terminated at level k if an undilute parcel rising from the first convective layer (I) is stable in layer $k + 1$. This happens when

$$(\theta_v^E)_{k+1} + b > \left[\theta_I^P + \frac{L_c}{c_p}\left\{q_I^P - q_s(\theta_{k+1}^E)\right\}\sigma_{k+1}^{-\kappa}\,\Pi^{-1}\right]\left\{1 + 0.61\,q_s(\theta_{k+1}^E)\right\}. \qquad \ldots (7.15)$$

This test prevents the detrainment from leading to excessive buoyancy.

Further testing of the column for convective instability is continued for the next layer above that where convection was terminated.

7.5. *Effects on the environment*

At those levels where convection has taken place the model's temperature and humidity fields are modified to take account of the changes in the nature of the environmental air. The latent heat released during condensation is added to the parcel temperature and so does not appear explicitly in the environmental heat budget. The changes described here are due to entrainment, detrainment and the subsidence which compensates for the parcel's upward mass flux. The effects of evaporation are considered in the next section.

For layer k the effects of the fluxes on the mass of the environmental air are

(i) *Entrainment:* a loss of

$$\left\{\frac{\varepsilon_{k-\frac{1}{2}}}{1+\varepsilon_{k-\frac{1}{2}}}+\varepsilon_{k+\frac{1}{2}}(1-\delta_k)(1-\eta_k)\right\}M_k$$

at the environmental values θ_k^{E} and q_k^{E}. In the lowest convective layer there is a loss of M_k at the initial values $\theta_k^{\mathrm{E}}+s_\theta$ and $q_k^{\mathrm{E}}+s_{\mathrm{q}}$ and a loss of $\varepsilon_{k-\frac{1}{2}}M_k$ at the environmental values of θ_k^{E} and q_k^{E}.

(ii) *Mixing detrainment:* a gain of $\eta_k M_k$ at the parcel values θ_k^{P} and q_k^{P}.

(iii) *Forced detrainment:* a gain of $\delta_k(1-\eta_k)M_k$ at the detrainment values θ_k^{R} and $\gamma_k q_{\mathrm{s}}(\theta_k^{\mathrm{R}})+(1-\gamma_k)q_k^{\mathrm{P}}$, except in the top layer where values θ_k^{P} and q_k^{P} are used.

(iv) *Downward mass flux into layer k:* a gain of $(1+\varepsilon_{k+\frac{1}{2}})(1-\delta_k)(1-\eta_k)M_k$ at the environmental values $\theta_{k+1}^{\mathrm{E}}$ and q_{k+1}^{E}.

(v) *Downward mass flux out of layer k:* a loss of $M_k/(1+\varepsilon_{k-\frac{1}{2}})$ at the environmental values θ_k^{E} and q_k^{E}. Note that this flux will be zero in the bottom convective layer.

On combining the effects (i)–(v) the net change in the values of the environmental potential temperature and specific humidity at level k may be calculated. These are given by

$$\Delta\theta_k=\frac{M_k}{\Delta\sigma_k}\{(1+\varepsilon_{k+\frac{1}{2}})(1-\delta_k)(1-\eta_k)(\theta_{k+1}^{\mathrm{E}}-\theta_k^{\mathrm{E}})+ \\ +\delta_k(1-\eta_k)(\theta_k^{\mathrm{R}}-\theta_k^{\mathrm{E}})+\eta_k(\theta_k^{\mathrm{P}}-\theta_k^{\mathrm{E}})\} \quad \ldots (7.16)$$

$$\Delta q_k=\frac{M_k}{\Delta\sigma_k}\{(1+\varepsilon_{k+\frac{1}{2}})(1-\delta_k)(1-\eta_k)(q_{k+1}^{\mathrm{E}}-q_k^{\mathrm{E}})+ \\ +\delta_k(1-\eta_k)(q_k^{\mathrm{R}}-q_k^{\mathrm{E}})+\eta_k(q_k^{\mathrm{P}}-q_k^{\mathrm{E}})\} \quad \ldots (7.17)$$

7.6. *Condensation, evaporation and precipitation*

Detrained cloud water is evaporated into the environment. This leads to further environmental temperature and humidity increments of the form

$$\Delta q_k=\{\delta_k+\eta_k(1-\delta_k)\}\frac{M_k X_k^{\mathrm{P}}}{\Delta\sigma_k} \quad \ldots (7.18)$$

$$\Delta\theta_k=-\frac{L_{\mathrm{c}}}{c_p}\Delta q_k. \quad \ldots (7.19)$$

Here X_k^{P} is the mixing ratio of cloud water at level k predicted by

$$X_{k+1}^{\mathrm{P}}=\frac{X_k^{\mathrm{P}}}{(1+\varepsilon_{k+\frac{1}{2}})(1+\varepsilon_{k+\frac{3}{2}})}+\gamma_{k+1}\{q_{k+1}^{\mathrm{P}}-q_{\mathrm{s}}(\theta_{k+1}^{\mathrm{P}})\} \quad \ldots (7.20)$$

and $\gamma_k=1$ if $q_k^{\mathrm{P}}>q_{\mathrm{s}}(\theta_k^{\mathrm{P}})$; otherwise $\gamma_k=0$.

Observations of summer convection (Ludlam 1980) suggest that precipitation does not occur until clouds attain a substantial depth. This depends on the aerosol size spectrum and is much greater for nucleus-rich continental air than for maritime air which has fewer but typically larger nuclei. At low temperatures, on the other hand, ice crystal growth through

the Bergeron–Findeisen process allows precipitation to form more readily and winter showers often result from quite shallow clouds. The convection scheme takes account of these effects by inhibiting precipitation unless the cloud depth, D_k, measured from the bottom of the first convective layer with a saturated parcel to the top of layer k, exceeds a critical value, D_{crit}. The values used for D_{crit} are based on Ludlam's (1980) data:

$$D_{\text{crit}} = \begin{cases} 4\,\text{km over land points} \\ 1.5\,\text{km over sea points} \\ 1\,\text{km if } T_{k+1} < 263\,\text{K}. \end{cases} \quad \ldots (7.21)$$

After fall-out of precipitation commences, some water is retained in the cloud by specifying a minimum cloud water content, X_{MIN}. This is taken as 1g kg^{-1} or the local saturation specific humidity where it is less.

Condensation of cloud water occurs if $D_k > D_{\text{crit}}$ and $X_k^{\text{P}} > X_{\text{MIN}}$. This is assumed to be immediately converted into precipitation. The amount produced, in millimetres per unit area, by taking the ensemble from level k to $k + 1$ is given by

$$P_k = (X_{k+1}^{\text{P}} - X_{\text{MIN}})\, M_{k+1} \frac{10^2 p_*}{g}. \quad \ldots (7.22)$$

The initial phase of the precipitation formed in this layer is assumed to be snow provided that

$$\frac{1}{2}(T_k^{\text{E}} + T_{k+1}^{\text{E}}) < 263\,\text{K}.$$

The snow then falls until it reaches the highest level whose temperature is greater than 273 K where it is allowed to melt, the environmental temperature at this level being adjusted accordingly (see equation 6.6).

The total amount of precipitation, J, falling from the base of the convective cloud is then given by

$$J_{\text{base}} = \sum_{m=c_{\text{base}}}^{c_{\text{top}}} P_m \quad \ldots (7.23)$$

where c_{top} is the cloud top, as defined by section 7.4, and c_{base} is the cloud base; that is the first convecting layer for which $X^{\text{P}} > 0$.

The precipitation falling below cloud base is now evaporated at those levels where the precipitation is diagnosed as rain. No evaporation of falling snow is carried out. The formula assumes an evaporation rate proportional to $(q - q_s)$ kg kg^{-1}s^{-1}, derived from the Marshall–Palmer drop size distribution (Bennetts and Rawlins 1981, Liu and Orville 1969) and is constructed by integrating the fractional evaporation of the falling precipitation over a layer of depth dz. This is given by

$$\frac{\mathrm{d}J}{J} = \frac{(q - q_s)}{R_\ell} \rho \mathrm{d}z \quad \ldots (7.24)$$

where ρ is the density of air and R_ℓ (mm s^{-1}) is the local rate of rainfall. R_ℓ is estimated by assuming that the precipitation covers 10% of a grid box and that little change occurs in the rainfall rate between cloud base and the ground. It then follows that

$$R_\ell = \frac{10\, J_{\text{base}}}{\Delta t} \quad \ldots (7.25)$$

where Δt is the time-step.

On converting to model coordinates the formula is applied by first starting at the level below cloud base and examining each level of the model in turn down to the surface. If $q_k < q_s(T_k)$, that is the air is not saturated, the precipitated water, J_{k+1}, reaching level k is modified as

$$J_k = J_{k+1} \exp\left[-\Delta t\, p_* \Delta\sigma \left\{q_s(T_k) - q_k\right\}/(10^2\, J_{\text{base}}\, g)\right]. \quad \ldots (7.26)$$

7.7. *Energy considerations*

The final stage of the scheme ensures that the vertically integrated sum of potential, internal and latent energies, that is

$$\int_0^1 (c_p T + L_c q)\, \mathrm{d}\sigma \quad \ldots (7.27)$$

is conserved by the convective motions. The full environmental temperature increments are therefore adjusted so that

$$\sum_{m=1}^{\text{TOP}} (c_p \Delta T_m + L_c \Delta q_m)\, \Delta\sigma_m = 0. \quad \ldots (7.28)$$

This is done by reducing either the set of positive or negative temperature increments according to which sign has the largest magnitude for its vertical integral.

8. SURFACE AND BOUNDARY LAYER

The description of the transfer of heat, moisture and momentum through the earth's boundary layer by the process of vertical turbulent mixing is based on the scheme due to Richards (1980). The equations used are those for vertical diffusion with a variable eddy diffusion coefficient:

$$\frac{\partial u}{\partial t} = \frac{\partial}{\partial z}\left(K_M \frac{\partial u}{\partial z}\right) \quad \ldots (8.1)$$

$$\frac{\partial v}{\partial t} = \frac{\partial}{\partial z}\left(K_M \frac{\partial v}{\partial z}\right) \quad \ldots (8.2)$$

$$\frac{\partial q}{\partial t} = \frac{\partial}{\partial z}\left(K_E \frac{\partial q}{\partial z}\right) \quad \ldots (8.3)$$

$$\frac{\partial \theta}{\partial t} = \frac{\partial}{\partial z}\left(K_H \frac{\partial \theta}{\partial z}\right) \quad \ldots (8.4)$$

where K_M, K_H and K_E are the diffusion coefficients for momentum, heat and moisture respectively. Turbulent fluxes are represented in the form $F_X = -K\partial X/\partial z$ and are calculated at half-levels within the boundary layer. The problem of determining the effects of vertical exchanges within the boundary layer therefore reduces to that of specifying these fluxes. Note that the forecast model has up to four full levels within its boundary layer and

increments to u, v, q and θ due to turbulent fluxes are calculated for the bottom four levels of the model.

8.1. *Surface exchanges*

At the surface the fluxes are defined in terms of bulk aerodynamic formulae:

$$F_u = - C_D |\mathbf{v}_1| u_1 \quad \ldots (8.5)$$

$$F_v = - C_D |\mathbf{v}_1| v_1 \quad \ldots (8.6)$$

$$F_\theta = - C_H |\mathbf{v}_1| (\theta_1 - \theta_*) \quad \ldots (8.7)$$

$$F_q = \frac{- M_* C_E |\mathbf{v}_1| \{q_1 - q_s(\theta_*)\}}{M_{\text{crit}} (1 + \gamma C_H |\mathbf{v}_1|)} \quad \ldots (8.8)$$

where $|\mathbf{v}_1| = (u_1^2 + v_1^2)^{\frac{1}{2}}$ and C_D, C_H and C_E are drag and exchange coefficients.

In equations (8.5)–(8.8) the subscript 1 denotes values at the lowest model level, and $*$ denotes surface values. Over land, θ_* is predicted from a heat budget based on radiation, evaporation, sensible heat flux and heat flux from deeper soil layers, whilst over the sea, the surface temperature is held constant in time throughout a forecast. The form of the surface moisture flux additionally allows for seasonal and geographic variations in surface evaporation through a dependence on soil moisture content and a surface resistance to evaporation (Monteith 1973, Rowntree 1983, Carpenter 1977). In (8.8), the equation describing the surface moisture flux, M_* is the soil moisture content and M_{crit} is a critical value which represents an upper limit on the soil moisture content. At present M_{crit} is taken to be 5 cm (Priestley and Taylor 1972). When $q_s(\theta_*) < q_1$, that is when conditions exist for a turbulent transport of moisture from the atmosphere in the form of dew, M_* is assumed to be equal to M_{crit} irrespective of the type of the underlying surface. When $q_s(\theta_*) > q_1$, that is for evaporation into the atmosphere, $M_* = 0$ over arid land points and $0 \leqslant M_* \leqslant M_{\text{crit}}$ over temperate land points. The surface resistance to evaporation, γ, is currently set to $60\,\text{s}\,\text{m}^{-1}$ and represents the effects of the interception and retention of surface moisture by vegetation. Note that $M_* = M_{\text{crit}}$ and $\gamma = 0$ over sea, snow and ice points. The model's surface land types are 'snow-covered', 'ice-covered', 'temperate' and 'arid'. These are specified from monthly climatology.

C_D, C_H and C_E depend on the roughness length z_0 (specified as 10^{-4} m over sea and 10^{-1} m over land) and the bulk Richardson number $(Ri)_B$ where

$$(Ri)_B = \frac{g z_1}{|\mathbf{v}_1|^2} \left[\frac{\theta_1 - \theta_*}{\theta_1} + 0.61 \frac{M_*}{M_{\text{crit}}} \{q_1 - q_s(\theta_*)\} \right] \quad \ldots (8.9)$$

and z_1 is the height of the bottom level. The forms taken by C_D, C_H and C_E can be seen from Figures 7 and 8. Note that $C_H = C_E$ is assumed throughout. Tabulated values of C_D and C_H are required near $(Ri)_B = 0$. These are derived from the similarity theory of Monin and Obukhov (1954), which gives

$$C_H = \frac{k^2}{\displaystyle\int_{\zeta_0}^{\zeta} \psi_M(\xi) \frac{d\xi}{\xi} \int_{\zeta_0}^{\zeta} \psi_H(\xi) \frac{d\xi}{\xi}} \quad \ldots (8.10)$$

$$C_D = \frac{k^2}{\left\{\int_{\zeta_0}^{\zeta} \psi_M(\xi)\frac{d\xi}{\xi}\right\}^2} \quad \ldots (8.11)$$

where $\zeta = z_1/\mathscr{L}$, $\zeta_0 = z_0/\mathscr{L}$, $k = 0.4$ is Kármán's constant and $\mathscr{L}$ is the Monin–Obukhov length. The form used for $\mathscr{L}$ follows from the assumption that z_0 is the same for momentum, heat and moisture exchanges (Carson and Richards 1978);

$$\mathscr{L} = \frac{C_D^{\frac{3}{2}}}{k\, C_H (Ri)_B} z. \quad \ldots (8.12)$$

ψ_M and ψ_H $(=\psi_E)$ are the Monin–Obukhov similarity functions defined by

$$\frac{\partial X}{\partial z} = \frac{X_*}{kz}\psi_X\left(\frac{z}{\mathscr{L}}\right). \quad \ldots (8.13)$$

X_* is a scaling value for X $(=u, v, \theta$ or $q)$ in the surface layer defined by

$$X_* = -F_X/u_*, \quad \ldots (8.14)$$

where u_* is the surface friction velocity.

The expressions used for ψ_H and ψ_M in stable conditions $(z/\mathscr{L} > 0)$ are due to Webb (1970):

$$\psi_M = \psi_H = \begin{cases} (1 + 5z/\mathscr{L}) & \text{for } 0 < z/\mathscr{L} \leqslant 1 \\ 6 & \text{for } 1 < z/\mathscr{L} < 6 \end{cases}. \quad \ldots (8.15)$$

The extension to highly stable conditions follows Carson and Richards (1978) and has a

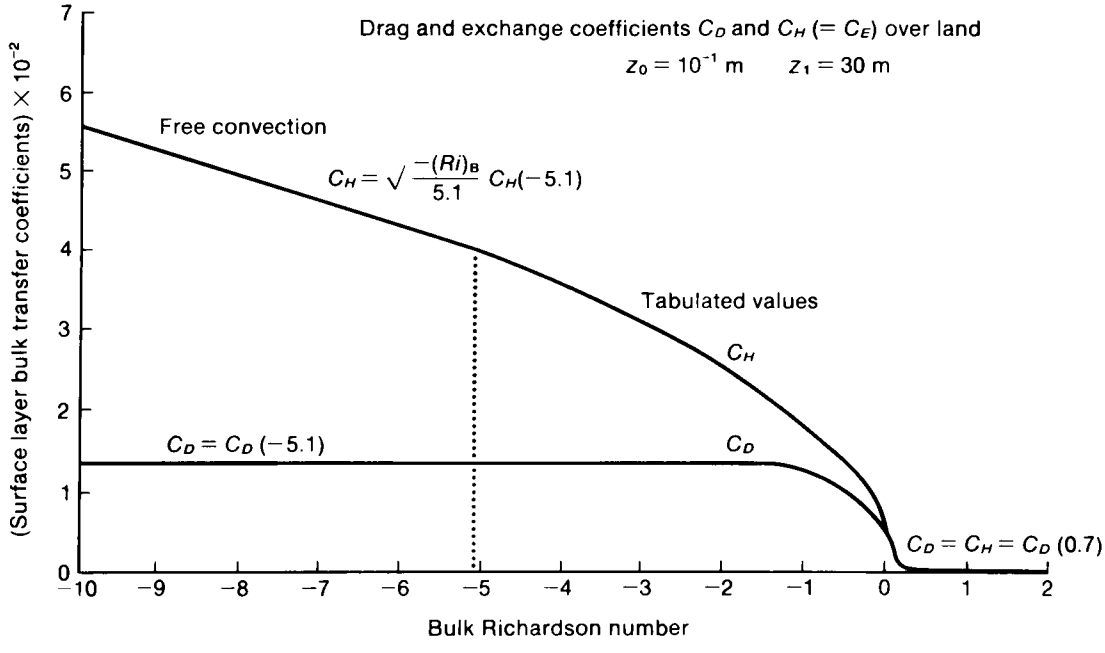

FIGURE 7. Surface layer bulk transfer coefficients used over land in the operational model. See text for details.

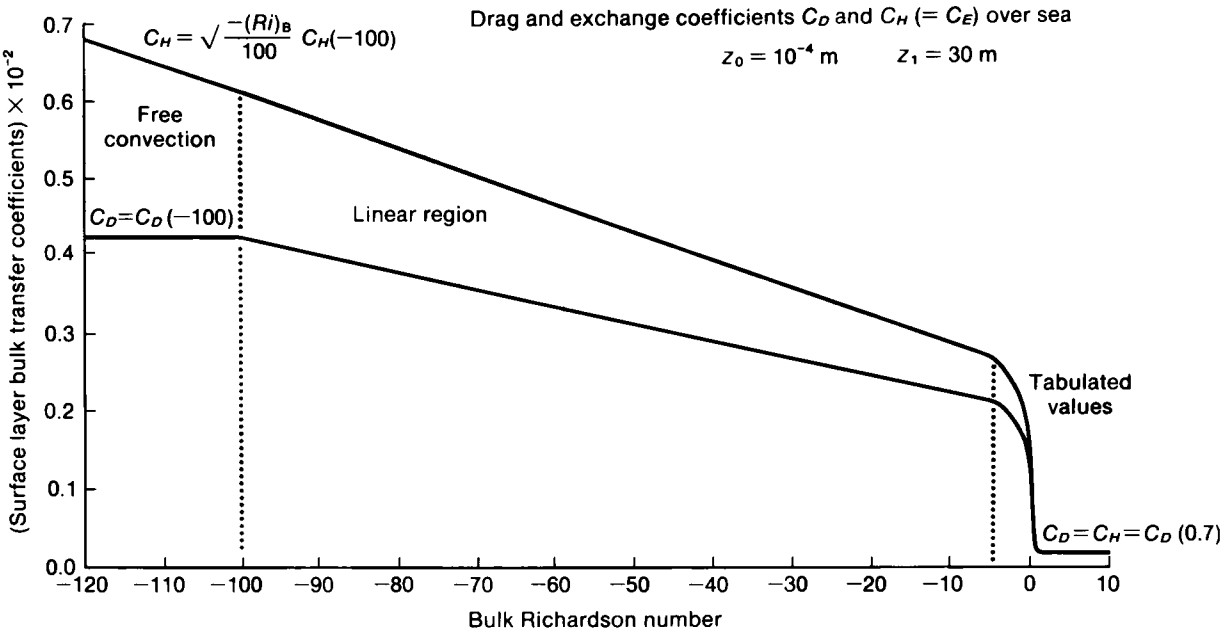

FIGURE 8. Surface layer bulk transfer coefficients used over sea in the operational model. See text for details.

lower limit set for C_H and C_D which applies for all $(Ri)_B$ greater than 0.7. In unstable and neutral conditions ($z/\mathscr{L} \leqslant 0$) ψ_H and ψ_M take the form (Dyer and Hicks 1970):

$$\psi_M = (1 - 16\, z/\mathscr{L})^{-\frac{1}{4}} \qquad \ldots (8.16)$$

$$\psi_H = (1 - 16\, z/\mathscr{L})^{-\frac{1}{2}}. \qquad \ldots (8.17)$$

These formulae are limited to $0 \geqslant z/\mathscr{L} \geqslant -1$. For more unstable conditions another approach, based on dimensional analysis in the so-called 'free convection limit', is used (Carson 1982). Over the sea, a smooth transition between the tabulated and free convection regimes is achieved by assuming a linear profile.

8.2 *Vertical diffusion*

Within the remainder of the boundary layer the fluxes take the form

$$F_X = -K_X \frac{\partial X}{\partial z} \qquad \ldots (8.18)$$

where K_X, a diffusion coefficient for variable X, depends on the depth of the boundary layer z_b, the Richardson number Ri, and the velocity gradient $|\partial \mathrm{v}/\partial z|$ through a mixing length formula such that

$$K_X = \ell^2 f_X(Ri)\, |\partial \mathrm{v}/\partial z| \qquad \ldots (8.19)$$

where f_X is a stability function and ℓ is the mixing length, the local Richardson number being given by

$$Ri = \frac{g}{T} \frac{\partial\theta/\partial z}{|\partial \mathbf{v}/\partial z|^2}. \qquad \ldots (8.20)$$

Note that in equation (8.20), the square of the vertical shear in the denominator is computed as $|\delta_z \mathbf{v}|^2/(\Delta z)^2$ and $|\delta_z \mathbf{v}|_{k+\frac{1}{2}}$ is not allowed to fall below $1/\Delta z_{k+\frac{1}{2}}$ where $\Delta z_{k+\frac{1}{2}} = z_{k+1} - z_k$.

The form chosen for the mixing length is

$$\ell = \left(\frac{1}{kz} + \frac{1}{\ell_A}\right)^{-1} \qquad \ldots (8.21)$$

and is due to Blackadar (1975). Here z is the height of the half-level at which K_X is being calculated and k is Kármán's constant. The asymptotic mixing length, ℓ_A, is given by

$$\ell_A = 0.089\, z_b \qquad \ldots (8.22)$$

where z_b is in metres.

The form of the stability function $f_X(Ri)$ is based on that given by Hicks (1976) for $Ri > 0$ and Dyer and Hicks (1970) for $Ri \leqslant 0$:

$$f_u(Ri) = f_v(Ri) = \left\{ \begin{array}{ll} (1 - 16\,Ri)^{\frac{1}{2}} & \text{if } Ri \leqslant 0 \\ (1 - 5\,Ri)^2 & \text{if } 0 < Ri \leqslant 0.143 \\ 0.009546\,(Ri^{-1} + 0.624) & \text{if } 0.143 < Ri < 1.3183 \\ 0 & \text{if } Ri \geqslant 1.3183 \end{array} \right\}. \qquad \ldots (8.23)$$

For the fluxes of θ and q, the form of $f_X(Ri)$ is the same as in (8.23) except in the unstable case, where

$$f_\theta(Ri) = f_q(Ri) = (1 - 16\,Ri)^{\frac{1}{2}} \quad \text{if} \quad Ri \leqslant 0. \qquad \ldots (8.24)$$

Fluxes and hence K_X, $f_X(Ri)$ and Ri are calculated at model half-levels. The vertical finite differences used are therefore calculated between full levels. The term z_b is defined to be the height of the lowest half-level at which the vertical heat fluxes fall to zero; that is, when $Ri \geqslant 1.3183$.

8.3. *Changes to the surface temperature*

The surface temperatures for land ice, sea ice and land points are calculated from the residual of the surface energy balance equation

$$G_* = R_* - H_* - Q_* \qquad \ldots (8.25)$$

where R_* is the surface net radiation (see section 9), H_* is the surface sensible heat flux, Q_* is the latent heat flux due to surface evaporation or sublimation by turbulent transfer and G_* represents the flux of heat into the soil at the surface. The latent and sensible heat fluxes are determined from

$$H_* = \rho_* c_p F_\theta \qquad \ldots (8.26)$$

$$Q_* = \rho_* L F_q \qquad \ldots (8.27)$$

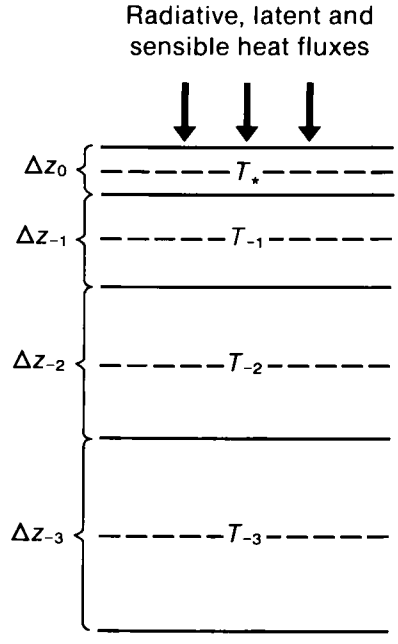

FIGURE 9. The four layers, Δz, used in the deep-soil temperature prediction scheme, where $\Delta z_0 = 0.055\,\text{m}$, $\Delta z_{-1} = 0.214\,\text{m}$, $\Delta z_{-2} = 0.599\,\text{m}$ and $\Delta z_{-3} = 1.378\,\text{m}$

where ρ_* is the density of air at the surface ($= p_* 10^2/(RT_*)\,\text{kg m}^{-3}$) and L is the appropriate latent heat for evaporation (including that of melting snow if $T_* \leqslant 273\,\text{K}$).

Over land ice and land points the flux of heat between the surface and deeper soil layers is modelled following Warrilow *et al.* (1986) by assuming that the evolution of temperature obeys a simple diffusion equation. This is represented by a four-layer model as shown in Figure 9. The depths of the layers have been chosen so that the system responds to both daily and seasonal forcing. Temperature is predicted for the top three soil layers with the bottom-most layer being held constant throughout a forecast according to seasonal climatology. The predictive equations take the form

$$\frac{\partial T_*}{\partial t} = \frac{G_*}{c_*} + \frac{2K}{\Delta z_0\,(\Delta z_0 + \Delta z_1)}(T_{-1} - T_*) \qquad \ldots (8.28)$$

$$\frac{\partial T_{-1}}{\partial t} = \frac{-2K}{\Delta z_{-1}\,(\Delta z_{-1} + \Delta z_0)}(T_{-1} - T_*) + \frac{2K}{\Delta z_{-1}\,(\Delta z_{-1} + \Delta z_{-2})}(T_{-2} - T_{-1}) \qquad \ldots (8.29)$$

$$\frac{\partial T_{-2}}{\partial t} = \frac{-2K}{\Delta z_{-2}\,(\Delta z_{-2} + \Delta z_{-1})}(T_{-2} - T_{-1}) + \frac{2K}{\Delta z_{-2}\,(\Delta z_{-2} + \Delta z_{-3})}(T_{-3} - T_{-2}) \qquad \ldots (8.30)$$

where $c_* = 1.32 \times 10^5\,\text{J m}^{-2}\,\text{K}^{-1}$ is the volumetric heat capacity of the surface layer. The heat diffusion coefficient is taken to be $K = 7.5 \times 10^{-7}\,\text{m}^2\,\text{s}^{-1}$ except over ice or snow-covered land points, where a reduced value of $K = 2.66 \times 10^{-7}\,\text{m}^2\,\text{s}^{-1}$ is used for diffusion between the surface layer and the first soil layer. This models the insulating effects of snow.

Over sea-ice points the change in surface temperature is calculated from

$$\frac{\partial T_*}{\partial t} = \frac{G_*}{c_*}. \qquad \ldots (8.31)$$

If $T_* \leqslant 271.2$ K over sea ice it is relaxed towards that value using the formula

$$\frac{\partial T_*}{\partial t} = 5.0 \times 10^{-6}(271.2 - T_*). \qquad \ldots (8.32)$$

This represents the flux of heat through the sea ice from the water below.

8.4. *Stability considerations*

Equations (8.1)–(8.4) are solved in an explicit manner and it is necessary to limit the size of the fluxes given by the above scheme to the maximum allowable for computational stability. In atmospherically unstable conditions this constraint can lead to severe truncation of the surface fluxes when the bottom model layer is very thin, as is the case with the distribution of levels used in the operational model. A further step is therefore carried out which permits the proportion of the surface fluxes remaining beyond the maxima allowed for computational stability to be passed through the bottom level and attributed to the next level above.

A similar coupling of the bottom two layers of the model is also carried out in the deep convection scheme (see section 7). A dry convective adjustment of these layers is therefore performed if necessary to give a well-mixed layer in unstable conditions.

These steps may be summarized as follows:

(i) The vertical diffusion coefficient is limited by

$$K_X < (\Delta z_1 + \Delta z_2)(\Delta z_{1+\frac{1}{2}})/2\Delta t$$

for the first half-level and by

$$K_X < \Delta z_k \, \Delta z_{k+\frac{1}{2}}/2\Delta t$$

for the kth half-level.

(ii) The bottom-level fluxes are restricted by

$$|F_1| < \left| \frac{(X_1 - X_2)(\Delta z_1 + \Delta z_2)}{\Delta t} \right|$$

where Δz_1 and Δz_2 are the thicknesses of the 1st and 2nd layers.

(iii) The surface fluxes may be redistributed between the lowest two levels of the model. If

$$|F_1| > \frac{|(X_1 - X_*)\Delta z_1|}{\Delta t} \quad \text{and} \quad (X_1 - X_*)(X_2 - X_*) > 0,$$

where X_* is the surface value, then $F_1 - (X_1 - X_*)\Delta z_1/\Delta t$ is added to F_2.

If

$$|F_1| > \frac{|(X_1 - X_*)\,\Delta z_1|}{\Delta t} \quad \text{and} \quad (X_1 - X_*)(X_2 - X_*) < 0$$

then F_1 is reduced to $(X_1 - X_*)\Delta z_1/\Delta t$.

If

$$|F_2| > \frac{|(X_2 - X_1)\,\Delta z_1|}{\Delta t} \quad \text{and} \quad (X_1 - X_2)(X_* - X_2) > 0$$

then $F_2 - (X_2 - X_1)\Delta z_1/\Delta t$ is added to F_1.

If

$$|F_2| > \frac{|(X_2 - X_1)\,\Delta z_1|}{\Delta t} \quad \text{and} \quad (X_1 - X_2)(X_* - X_2) < 0$$

then F_2 is reduced to $(X_2 - X_1)\Delta z_1/\Delta t$.

(iv) The convective adjustment between the bottom two levels is applied when $\theta_1 > \theta_2$. All variables X are mixed so that

$$X_1 = X_2 = \frac{X_1\Delta\sigma_1 + X_2\Delta\sigma_2}{\Delta\sigma_1 + \Delta\sigma_2}$$

where $\Delta\sigma_1$ and $\Delta\sigma_2$ are the thickness of the 1st and 2nd levels.

9. RADIATION

Radiation calculations are performed using a scheme developed for use in general circulation studies, the most recent version is due to Slingo and Wilderspin (1984). Interactive cloud, diagnosed from the model's relative humidity field and convection scheme, is used to predict the effects on atmospheric heating of the reflection, absorption and emission of radiation. Four types of cloud are catered for in the scheme: high, medium and low layer cloud, and a convective tower. The layer clouds are assumed to be one sigma layer in thickness, but the convective cloud may occupy more than one sigma layer. The clouds overlap randomly in the vertical, except that where layer and convective clouds are present at the same level then the overlap of layer clouds occurs only in the clear air, after allowing for convective cloud. As a first approximation, convective cloud is pictured as a vertical column with no reflection or interaction by the sides with the surrounding air. Any short-wave radiation entering the cloud is assumed to pass straight through, after attenuation by the cloud, and emerge at the cloud base.

Three actively absorbing gases are considered in calculating the radiative heating rates: water vapour, carbon dioxide and ozone. However, the treatment of ozone is currently limited to the effects of solar absorption. The specific humidity of the model is assumed to describe the water vapour distribution and both the band absorption and the water vapour continuum are treated. Carbon dioxide is assumed to be well mixed throughout the atmosphere with a mixing ratio of $4.9 \times 10^{-4}\,\mathrm{kg\,kg^{-1}}$. Ozone mixing ratios are specified above 200 mb from monthly climatological zonally meaned values (Bolton 1981).

The radiation scheme is essentially divided into two parts: short wave and long wave. This is possible since there is very little overlap in wavelength between the incoming solar radiation and the outgoing terrestrial radiation. In each part, the fluxes are calculated at layer boundaries and, after the two contributions have been added, vertical differencing is used to obtain heating rates at the surface and at all layers of the model atmosphere. A full calculation of radiative fluxes is performed at regular intervals during the model integration with the radiative cooling and heating effects being meaned over the time until the next radiation calculation. The time between full radiation calculations is currently 3 hours, and the radiative heating rates are held constant during this time.

9.1. *Long-wave radiation*

Long-wave radiation is absorbed and emitted by atmospheric gases, clouds and the earth's surface. The absorption by water drops is so strong that most clouds in the lower troposphere absorb essentially all the incident long-wave flux and emit a flux which is similar to that for a black body at the cloud boundary temperature. Cloud radiative properties in the long-wave region are thus independent of wavelength for practical purposes. In contrast, the wavelength dependence of the absorption and emission by the radiatively active gases is very complex. This is because they have many vibrational and rotational energy transitions which may be excited by long-wave radiation. As a result, there are tens of thousands of spectral lines, grouped into a much smaller number of bands. The treatment of long-wave radiation thus requires a judicious division of the spectrum, such that these bands and the main regions of overlap between the contributions for the various gases are represented as accurately as possible. The spectral divisions and band limits used in the scheme are shown in Figure 10.

In the development of the theory we assume that there is only one cloud layer. The extension to several randomly overlapped cloud layers is straightforward. Note also that the contributions to the long-wave flux are calculated separately for each spectral band.

9.1.1. *Downward long-wave flux.* The total downward radiative flux $I^{\downarrow}$ at height z will, in general, have two components—the clear sky downward flux $I^{\infty\downarrow}$ and the downward flux from the cloud base $I^{C\downarrow}$: thus

$$I^{\downarrow}(z) = (1 - Q)\, I^{\infty\downarrow}(z) + QI^{C\downarrow}(z) \qquad \ldots (9.1)$$

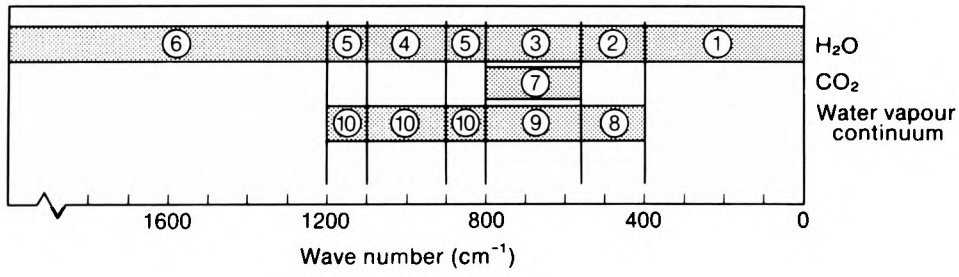

FIGURE 10. The spectral divisions and band limits used in the long-wave part of the radiation scheme. The numbers identify the separate contributions to the total flux from each of the absorbers listed on the right.

where Q is the cloud amount and $I^{\infty\downarrow}(z)$ is given by the radiative transfer equation

$$I^{\infty\downarrow}(z) = \int_0^\infty \{\pi B_\omega(T_z) - \pi B_\omega(T_\infty)\gamma_{i\omega}(z, \infty)\}\,\mathrm{d}\omega + \\ + \int_0^\infty \int_{T_z}^{T_\infty} \pi\gamma_{i\omega}(z, z')\frac{\mathrm{d}B_\omega(T_{z'})}{\mathrm{d}T_{z'}}\,\mathrm{d}T_{z'}\,\mathrm{d}\omega. \quad \ldots (9.2)$$

Here $\gamma_{i\omega}$ is the flux transmittance or transmission function for gas i at frequency ω, $B_\omega(T)$ is the Planck function at frequency ω and temperature T, and T_∞ is the temperature at the top of the atmosphere.

The flux transmittance is given by

$$\gamma_{i\omega}(z, z') = 2\int_0^{\pi/2} \exp\left\{-\int_0^{y_i(z,z')} x_{i\omega}\sec\xi\,\mathrm{d}Y\right\}\sin\xi\cos\xi\mathrm{d}\xi \quad \ldots (9.3)$$

where $x_{i\omega}$ is the extinction coefficient at frequency ω for gas i, ξ is the zenith angle and the optical path length, $y_i(z, z')$ is given by

$$y_i(z, z') = \int_0^{z'} \rho_i(\zeta)\mathrm{d}\zeta - \int_0^z \rho_i(\zeta)\mathrm{d}\zeta = Y(z') - Y(z) \quad \ldots (9.4)$$

where $\rho_i(\zeta)$ is the density of gas i at height ζ.

$I^{C\downarrow}(z)$ is the downward flux from the cloud base. All clouds are assumed to be black bodies, apart from high cloud which is assumed to be 'grey'. This is effected by multiplying the high cloud amount by its emissivity, 0.75, and then treating it as a black body. $I^{C\downarrow}(z)$ is given by

$$I^{C\downarrow}(z) = \int_0^\infty \pi B_\omega(T_{\text{base}})\mathrm{d}\omega + \int_0^\infty \int_{T_z}^{T_{\text{base}}} \pi\gamma_{i\omega}(z, z')\frac{\mathrm{d}B_\omega(T_{z'})}{\mathrm{d}T_{z'}}\,\mathrm{d}T_{z'}\,\mathrm{d}\omega \quad \ldots (9.5)$$

where T_{base} is the temperature at cloud base.

To perform the spectral integration in (9.2) and (9.5) we make use of the emissivity approximation. The spectrum is split into bands over which the emissivity and absorptivity are assumed to have no frequency dependence. We define partial emissivity as

$$\varepsilon_i(\omega_1, \omega_2; z, z') = \frac{\int_{\omega_1}^{\omega_2} B_\omega\{1 - \gamma_{i\omega}(z, z')\}\,\mathrm{d}\omega}{\int_{\omega_1}^{\omega_2} B_\omega\,\mathrm{d}\omega} \quad \ldots (9.6)$$

and partial absorptivity as

$$\bar{\varepsilon}_i(\omega_1, \omega_2; z, z') = \frac{\int_{\omega_1}^{\omega_2} \frac{\mathrm{d}B_\omega}{\mathrm{d}T}\{1 - \gamma_{i\omega}(z, z')\}\,\mathrm{d}\omega}{\int_{\omega_1}^{\omega_2} \frac{\mathrm{d}B_\omega}{\mathrm{d}T}\mathrm{d}\omega} \quad \ldots (9.7)$$

where ω_1 and ω_2 are the frequencies defining the limits of a band. On writing

$$\int_{\omega_1}^{\omega_2} B_\omega(T)\,\mathrm{d}\omega = b_{12}(T) \qquad \ldots (9.8)$$

equations (9.2) and (9.5) become

$$I^{\infty\downarrow}(z) = \sum_{\text{Bands}} \pi\varepsilon_i(\omega_1, \omega_2; z, \infty)\, b_{12}(T_\infty) - \pi \int_{b_{12}(T_z)}^{b_{12}(T_\infty)} \bar{\varepsilon}_i(\omega_1, \omega_2; z, z')\,\mathrm{d}b_{12}(T_{z'}) \qquad \ldots (9.9)$$

and

$$I^{\mathrm{C}\downarrow}(z) = \sum_{\text{Bands}} \pi b_{12}(T_{\text{base}}) - \pi \int_{b_{12}(T_z)}^{b_{12}(T_{\text{base}})} \bar{\varepsilon}_i(\omega_1, \omega_2; z, z')\,\mathrm{d}b_{12}(T_{z'}). \qquad \ldots (9.10)$$

Note that the first term here is

$$\pi \int_0^\infty B_\omega(T_{\text{base}})\,\mathrm{d}\omega = CT_{\text{base}}^4,$$

where C is Stefan's constant. The Planck function integral (9.8) is calculated by a cubic in temperature for each of the six bands. This was obtained by numerical integration of the Planck function using a 1 cm^{-1} spectral resolution for 5 K intervals from 180 K to 320 K.

9.1.2. *Upward long-wave flux.* As in (9.1) the total upward radiative flux $I^\uparrow$ at height z will, in general, have two components—the clear sky upward flux from the surface of the earth $I_\bullet^{\infty\uparrow}$ and the upward flux from the cloud top $I^{\mathrm{C}\uparrow}$: thus

$$I^\uparrow(z) = (1 - Q)\, I_\bullet^{\infty\uparrow}(z) + QI^{\mathrm{C}\uparrow}(z), \qquad \ldots (9.11)$$

$$I_\bullet^{\infty\uparrow}(z) = CT_\bullet^4 + \sum_{\text{Bands}} \int_{b_{12}(T_\bullet)}^{b_{12}(T_z)} \pi\,\bar{\varepsilon}_i(\omega_1, \omega_2; z', z)\,\mathrm{d}b_{12}(T_{z'}) \qquad \ldots (9.12)$$

and $I^{\mathrm{C}\uparrow}(z)$ the upward flux from the cloud top, which is given by an equation identical to (9.12) but with T_{top} (the cloud-top temperature) replacing $T_\bullet$.

9.1.3. *Overlaps.* For bands 2–5 the absorption spectra of the gases overlap (Figure 10), and so it is not possible to split the spectrum into bands for which just one gas is active. An approximate partial absorptivity and emissivity for the overlap is calculated from the absorptivities and emissivities for the individual gases. We set:

$$\bar{\varepsilon} \approx 1 - \prod_{\text{Gases}} (1 - \bar{\varepsilon}_i) \qquad \ldots (9.13)$$

$$\varepsilon \approx 1 - \prod_{\text{Gases}} (1 - \varepsilon_i). \qquad \ldots (9.14)$$

Equation (9.14) is written in this manner because the absorptivity is actually calculated from a table of transmissivities, defined by

$$\bar{\tau} = (1 - \bar{\varepsilon}). \qquad \ldots (9.15)$$

9.1.4. *Line absorption.* The dependence of the emissivities and absorptivities on temperature and pressure through line absorption by water vapour and carbon dioxide is parametrized through a scaling of the path length.

The variation with pressure of the extinction coefficient $x_{i\omega}$ (see equation 9.3) is modelled by using a pressure weighting of the path length (Houghton 1977) to give an effective optical depth:

$$\bar{y}_i(z, z') = \int_{Y(z)}^{Y(z')} \left(\frac{p}{p_0}\right)^{w_i} \mathrm{d}Y \qquad \ldots (9.16)$$

where p is the pressure, p_0 is standard atmospheric pressure (1013.25 mb), w_i is the pressure scaling factor for gas i and Y is as defined in equation 9.4. On assuming that the humidity mixing ratio, which is approximately equal to the specific humidity, $(q_i)_k$ of gas i is constant in a layer k we approximate (9.16) by

$$(\bar{y}_i)_k = (q_i)_k p_* \left(\frac{p_*}{p_0}\right)^{w_i} \frac{10}{g} \frac{1}{(1 + w_i)} \left\{\sigma_{k+\frac{1}{2}}^{(1+w_i)} - \sigma_{k-\frac{1}{2}}^{(1+w_i)}\right\}. \qquad \ldots (9.17)$$

Where $(\bar{y}_i)_k$ is expressed in g cm^{-2} and w_i is taken to be 0.9 for both water vapour and carbon dioxide.

The variation of the extinction coefficient with temperature along an atmospheric path is ignored for water vapour but parametrized for carbon dioxide (Slingo and Wilderspin 1984) by scaling the path length in layer k by a factor

$$\left(\frac{T_k}{263}\right) \max \{8.5 + 2 \log_{10} (\bar{y}_i)_k, 0\}. \qquad \ldots (9.18)$$

This scaling assumes that the emissivity at any temperature T may be expressed in terms of observed values for 263 K. It was derived by fitting data obtained by applying the version of the Goody (1964) random-band model described by Hunt and Mattingly (1976) to Air Force Geophysics Laboratory data (Rothman 1981).

9.1.5. *Water vapour continuum absorption.* The treatment of the water vapour continuum absorption follows that of Slingo and Wilderspin (1984) and includes the strong temperature dependence of the so-called e'-type absorption (e' is the water vapour partial pressure). The distinction between emissivity and absorptivity is ignored (see definitions (9.6) and (9.7)) and the transmissivity is taken to follow an exponential law, which is usually written as

$$\bar{\tau} = \exp \{- v (j_1 p + j_2 e')\} \qquad \ldots (9.19)$$

where v is the water vapour absorber amount and p is pressure (taken as 1013 mb). The broadening coefficient j_1 arises from broadening of water vapour lines by collisions with other gases. The e'-type coefficient j_2 is often stated to represent the effect of the dimer molecule $(H_2O)_2$.

On using the approximation $q = 0.622e'/p$ and substituting for the amount of water vapour absorber in layer k, the emissivity and absorptivity are given by

$$\varepsilon_k = \bar{\varepsilon}_k = D_f q_k \Delta\sigma_k p_* \frac{10}{g} \frac{\sigma_k p_*}{1013} \left(1 + \frac{j_2}{j_1} \frac{q_k}{0.622}\right). \qquad \ldots (9.20)$$

Here D_f is the diffusivity factor taken to be 1.66, and j_1/j_2 is taken to be 0.005 in all three

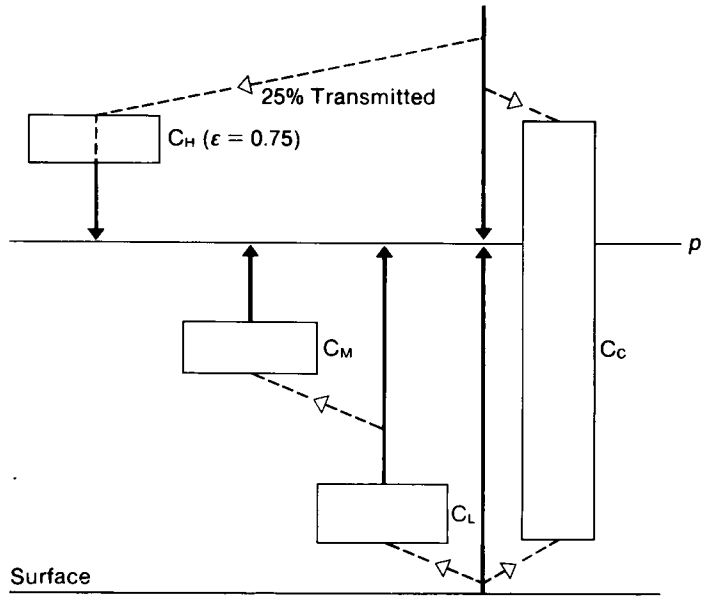

FIGURE 11. Long-wave fluxes at pressure level, p, in a cloudy atmosphere. For high cloud, C_H, emissivity, ε, equals 0.75, otherwise the fluxes incident on each cloud (dashed lines) are assumed to be totally absorbed.

bands which include the continuum. In addition, the treatment of the temperature dependence of j_2 given by Roberts *et al.* (1976) is included by setting

$$j_2(T) = j_2(296\,\mathrm{K}) \exp\left(\frac{1800}{T} - \frac{1800}{296}\right). \quad \ldots (9.21)$$

The values of j_1 in bands 2–5 (terms 8–10 in Figure 10) are taken to be 0.35×10^{-5}, 0.15×10^{-5} and $0.05 \times 10^{-5}\,\mathrm{kg^{-1}\,m^2\,atm^{-1}}$.

9.1.6. *Clouds.* Clouds have a dominating effect on thermal emission just as they do for solar radiation. When they are present the long-wave flux to space is reduced since they block the surface flux and emit at a temperature that is lower than that of the earth's surface. Similarly the downward surface flux is increased since the cloud radiates at a higher temperature than the equivalent black-body temperature of the radiation from clear air. Thus from the long-wave standpoint both the atmosphere and the surface tend to warm.

The effect of a typical cloud configuration on the infra-red fluxes is shown in Figure 11. The upward and downward fluxes each divide into five components, associated with each type of cloud and through the clear air either from space or from the surface. The surface is assumed to act as a black body so that the downward flux at the ground is completely absorbed. With the exception of high cloud which has an emissivity of 0.75, all clouds are treated as perfect absorbers and emitters of infra-red radiation. In the scheme a cloud is assumed to be active with respect to thermal radiation only near its upper or lower boundary, so that as a first approximation the thermal radiation leaving through the cloud surface can be identified with the black-body emission at the temperature of the cloud boundary.

9.2. *Solar radiation*

9.2.1. *Incoming radiation.* The formula used to calculate the incoming solar radiation, S, reaching the top of the earth's atmosphere takes account of the eccentricity of the earth's orbit:

$$S = S_p \{(1 + e \cos \Omega_p)/(1 - e^2)\}^2 \quad \ldots (9.22)$$

where S_p is the solar constant at perihelion (1395 W m^{-2}), e is the eccentricity of the earth's orbit (0.0167), and Ω_p is the angular distance from perihelion (January 3), assumed to vary linearly with time.

To determine the incoming radiation at any location the solar zenith angle, ξ, must be found. This is given by

$$\cos \xi = \cos \phi \cos \delta \cos \tau_0 - \sin \phi \sin \delta \quad \ldots (9.23)$$

where ϕ is latitude, δ is the solar declination and $\tau_0 = \lambda + \pi(t - 12)/12$ is the hour angle of the sun. Here λ is longitude and t is GMT measured in hours.

As radiation increments cannot be calculated every time-step, the effects of solar radiation are meaned over the time between radiation calls by calculating a mean cosine of zenith angle:

$$\overline{\cos \xi} = \frac{\int_{h_1}^{h_2} (\cos \phi \cos \delta \cos \tau_0 - \sin \phi \sin \delta) \, d\tau}{h_2 - h_1} \quad \ldots (9.24)$$

where h_1 and h_2 are the hour angles either for the time between radiation calls or for sunrise or sunset, whichever is appropriate.

The solar constant is further reduced by a factor 0.97 as an approximation of Rayleigh scattering.

9.2.2. *The flux of solar radiation.* The total downward solar flux $S^{\downarrow}$ at height z will, in general, have two components—the direct, clear sky flux $S^{\infty\downarrow}$ and the diffuse flux from the cloud $S^{C\downarrow}$, thus

$$S^{\downarrow}(z) = (1 - Q) S^{\infty\downarrow}(z) + Q\Lambda S^{C\downarrow}(z) \quad \ldots (9.25)$$

where Λ is the transmissivity of the cloud. $S^{\infty\downarrow}(z)$ and $S^{C\downarrow}(z)$ are defined by

$$S^{\infty\downarrow}(z) = S \cos \xi \left[1 - \int_0^{\infty} A_{i\omega} \{X_m \bar{y}(z, \infty)\} \, G(\omega) \, d\omega \right] \quad \ldots (9.26)$$

$$S^{C\downarrow}(z) = S \cos \xi \left[1 - \int_0^{\infty} G(\omega) \, A_{i\omega} \{X_m \bar{y}(z_{top}, \infty) + D_f \bar{y}(z, z_{top})\} \, d\omega \right]. \quad \ldots (9.27)$$

Here S is the solar constant, z_{top} = height of cloud top, and $A_{i\omega}$ is the absorption of gas i at frequency ω. X_m is a magnification factor which takes account of the greater amount of atmosphere traversed when the zenith angle increases and is given (Houghton 1963) by:

$$X_m = \left(1 + \frac{z}{a}\right)\left(\frac{2z}{a} + \cos^2 \xi\right)^{-\frac{1}{2}} \quad \ldots (9.28)$$

where a is the radius of the earth, z is a height which is representative for ozone absorption and $z/a = 0.0078394$. Note that this reduces to $\sec \xi$ for small ξ.

In the above, $\bar{y}$ is the pressure weighted path length as given in (9.16), the scaling being only applied for water vapour, for which $w_i = 0.9$. The diffusivity factor, D_f, is taken to be 1.66 (Liou 1980), and $G(\omega)$ describes the frequency variation of the solar beam at the top of the atmosphere.

The frequency integration is again performed by splitting the spectrum into bands. This time only three bands are required, one for carbon dioxide, one for water vapour and one for ozone. There is no significant overlap between the absorption spectra of these gases, so the absorptions are simply added together. The variation of the absorption with the amount of absorber gas is taken from Manabe and Möller (1961).

The reflected solar beam receives an extremely simple treatment in that it is reflected straight to space without absorption in its upward path. Cloud optical properties are listed in Table XI and the effects of clouds on the solar beam are illustrated in Figure 12.

The surface albedo, α, is specified geographically. Snow-free land grid points have values between 0.11 and 0.35 depending on surface type. For sea points $\alpha = 0.06$, and points where the climatological surface type is determined as snow covered or ice covered are assigned higher values of 0.5 and 0.8 respectively. The surface albedo is changed to take account of multiple reflections between cloud and ground (see Figure 13). The effective surface albedo is defined as:

$$\alpha_{\text{eff}} = \alpha(1 - \overline{Q}\,\overline{\beta})/(1 - \alpha\overline{Q}\,\overline{\beta}) \qquad \ldots (9.29)$$

where

$$\overline{Q} = 1 - \prod_{i=1}^{4}(1 - Q_i) \quad \text{and} \quad \overline{\beta} = \frac{\sum_{i=1}^{4} \beta_i S_i}{\sum_{i=1}^{4} S_i}$$

and Q_i is the amount of cloud type i, β_i is the reflectivity of cloud type i and S_i is the solar flux reaching the earth's surface from cloud type i.

9.3. *The calculation of heating rates*

We now have the upward and downward short-wave and long-wave fluxes available at layer boundaries. The contributions from the different parts of the spectrum are added, and the downward flux subtracted from the upward flux to give the net flux. We now calculate the heating rate in a layer to be

$$\frac{\partial T_k}{\partial t} = -\frac{g}{c_p}\frac{\partial \mathscr{R}_k}{\partial p} \approx -\frac{g}{c_p}\frac{(\mathscr{R}_{k+\frac{1}{2}} - \mathscr{R}_{k-\frac{1}{2}})}{p_*(\sigma_{k+\frac{1}{2}} - \sigma_{k-\frac{1}{2}})} \qquad \ldots (9.30)$$

and at the surface the heating rate is

$$\frac{\partial T_*}{\partial t} = \frac{\mathscr{R}_*}{c_*} \qquad \ldots (9.31)$$

where $\mathscr{R}_k$ is the net flux at level k.

TABLE XI. *Cloud optical properties*

Cloud type	Reflectivity	Transmissivity	Absorbtivity
High (C_H)	0.2	0.75	0.05
Medium (C_M)	0.6	0.3	0.1
Low (C_L)	0.6	0.3	0.1
Convective (C_C)	0.6	0.3	0.1

9.4. *The parametrization of cloud*

The cloud amounts Q are parametrized in a simple and computationally economical manner. Convective cloud amounts are calculated by scaling the convective mass flux against a theoretical maximum as discussed by Slingo J. M. (1980). The heights of the base and top of the convective tower are calculated within the convection scheme as described in section 7.6.

As noted previously, layer clouds are assumed to be one layer thick. In the absence of deep convection extending over more than five model levels, three layers of cloud can occur: low clouds in layers 2–4, medium clouds in layers 5–9 and high clouds in layers 10–12. Cloud amounts are estimated from the relative humidity, U, by the formula:

$$Q_{H,M,L} = \begin{cases} \dfrac{(U - U_{crit})^2}{(1 - U_{crit})} & U > U_{crit} \\ 0 & U \leqslant U_{crit} \end{cases} \quad \ldots (9.32)$$

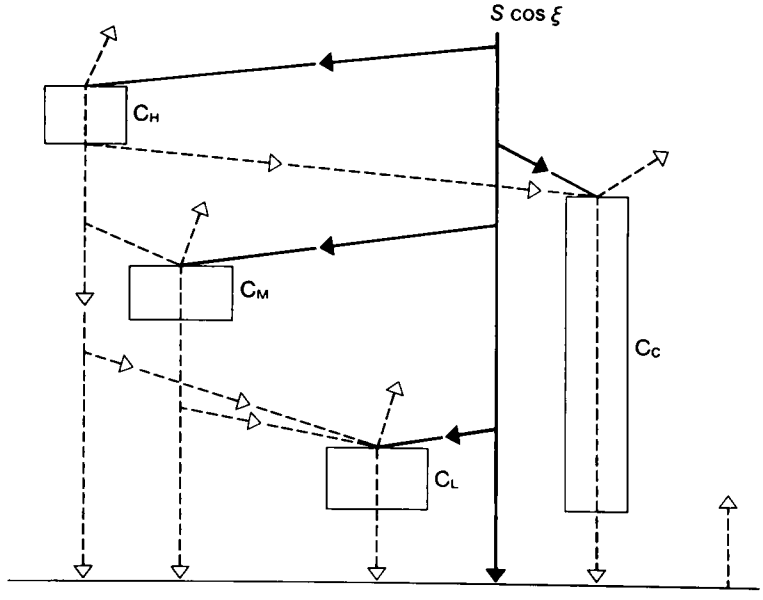

FIGURE 12. Division of the solar beam during its passage through a cloudy atmosphere. Solid lines indicate direct solar radiation, dashed lines diffuse solar radiation.

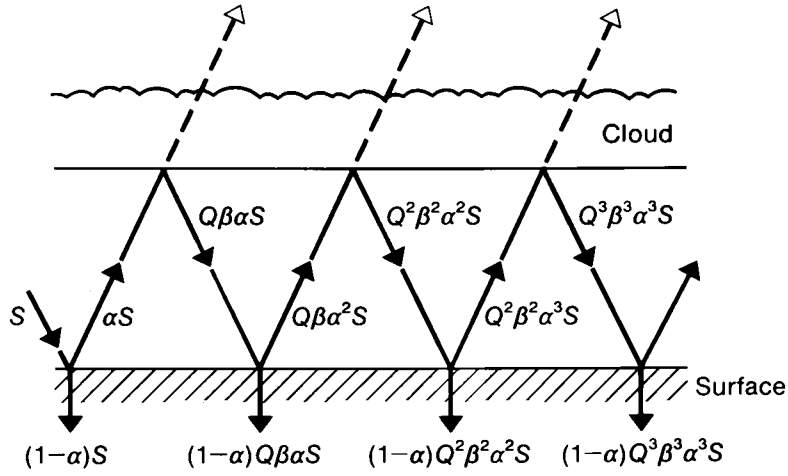

FIGURE 13. Multiple reflections between cloud and the surface. See text for explanation of symbols.

where $Q_{H,M,L}$ are amounts of high, medium and low cloud, U is expressed as a decimal fraction and U_{crit} is a critical relative humidity, taken to be 0.85. The maximum value taken by Q in each of the three bands of layers dictates the cloud amount and the cloud is assigned to those layers.

If deep convection is predicted, then the cloud base is assumed to be at the base of the convective tower, and the quadratic equation (9.32) is evaluated at that level only. Only 10% of the convective cloud is assumed to occupy the full depth, the remainder being added to the layer cloud amount.

An estimate of marine stratocumulus (Slingo J. M. 1980) is also included in the low cloud amount. If there is no surface inversion a further term Q_{sc} depending on the inversion strength is added to equation (9.32)

$$Q_{sc} = \begin{cases} -16.67\dfrac{\partial\theta}{\partial p} - 1.167 & U > 0.85, \dfrac{\partial\theta}{\partial p} \leqslant -0.07 \\ \left(-16.67\dfrac{\partial\theta}{\partial p} - 1.167\right)\dfrac{(U-0.5)}{0.35} & 0.85 \geqslant U > 0.5, \dfrac{\partial\theta}{\partial p} \leqslant -0.07 \\ 0 & \text{otherwise.} \end{cases} \quad \cdots (9.34)$$

10. GRAVITY-WAVE DRAG

Amongst others, Sawyer (1960), Lilly (1972) and Bretherton (1969) have presented evidence that an important mechanism for the transfer of momentum between the earth's surface and the atmosphere is the pressure drag on the atmosphere due to orographically induced gravity waves. These waves propagate upwards and interact with the mean flow, extracting momentum from the troposphere and stratosphere as they dissipate. The horizontal scale of these waves is sub-grid-scale and so they cannot normally be resolved by the model.

More recently Palmer *et al.* (1986) have shown that a simple representation of gravity-wave drag can have a beneficial effect on both numerical weather prediction models and general circulation models. A parametrization of gravity-wave drag based on the ideas of Palmer *et al.*, though different in some important respects, is now included in the model. In contrast to their Richardson number parametrization scheme, the calculation of the vertical distribution of wave momentum flux divergence is simplified by specifying it independently of the model profile. A critical level determined by the direction of the local wind is also assumed, beyond which the gravity waves are unable to propagate. The impact of this scheme on the forecast model is described by Kitchen *et al.* (1985).

10.1. *Surface momentum flux*

The effect of the vertical flux of gravity-wave momentum on the large-scale flow is determined by the equations

$$\frac{\partial u}{\partial t} = \frac{1}{\rho}\frac{\partial}{\partial z}(\rho\,\overline{w'u'}) \qquad \ldots (10.1)$$

$$\frac{\partial v}{\partial t} = \frac{1}{\rho}\frac{\partial}{\partial z}(\rho\,\overline{w'v'}) \qquad \ldots (10.2)$$

where (u, v) is the horizontal wind field, ρ the density of air and the covariances $\rho\overline{w'u'}$ and $\rho\overline{w'v'}$ represent the separate horizontal components of the vertical flux of momentum.

The surface momentum fluxes, $(\rho\overline{w'u'})_*$ and $(\rho\overline{w'v'})_*$, are estimated in terms of a typical value, τ_*. Their magnitude is assumed to be given by linear theory assuming a stationary wave solution in uniform flow (Palmer *et al.* 1986). This gives a relationship of the form

$$(\rho\overline{w'u'})_* = A_c\, u_2\, (\theta_3 - \theta_1)^{\frac{1}{2}}\, p_* H_V \tau_* \qquad \ldots (10.3)$$

with a similar equation for the meridional direction. Subscripts 1, 2 and 3 refer to values at those model levels. H_V is the sub-grid-scale variance of orographic height and A_c is a constant of proportionality. The value of H_V in equation (10.3) is limited by

$$H_V < (400)^2\ \mathrm{m}^2. \qquad \ldots (10.4)$$

This prevents the momentum flux taking unrealistically large values near major mountain ranges.

Using equation (10.3) the constant of proportionality, A_c, is given by requiring $(\rho\overline{w'u'})_* = \tau_* = 0.15\,\mathrm{N\,m^{-2}}$ under conditions for which $u_2 = 5\,\mathrm{m\,s^{-1}}$, $\theta_3 - \theta_1 = 10\,\mathrm{K}$ and with $p_* = 1000\,\mathrm{mb}$ $(10^5\,\mathrm{N\,m^{-2}})$ so that

$$A_c = 1/(5\sqrt{10\,\overline{H_V}\,10^5})\ \mathrm{s\,N^{-1}\,m^{-1}\,K^{-\frac{1}{2}}} \qquad \ldots (10.5)$$

where $\overline{H_V}$ is the global mean variance of the sub-grid-scale orography.

10.2. *Vertical distribution of the momentum flux*

The wave momentum flux at height z above the surface is assumed to be proportional to the surface flux. From equations (10.1) and (10.3) the deceleration of the zonal wind is therefore

given in finite-difference notation by

$$\frac{\partial u_k}{\partial t} = A_c u_2 (\theta_3 - \theta_1)^{\frac{1}{2}} p_* H_V \frac{1}{\rho_k} \frac{\Delta\tau(z_k)}{\Delta z_k} \quad \ldots (10.6)$$

where $\tau(0) = \tau_*$.

$\tau(z)$ describes the vertical distribution of the drag. In reality this probably depends on the local Richardson number, which in turn is a function of the fine structure of u and θ in the vertical profile, since the gravity waves may be dissipated by convective overturning or shear instability (Fritts 1984). Since this is difficult to estimate, a simple approach is used at present by assuming that

$$\frac{\partial\tau}{\partial p} = \gamma_d \quad \ldots (10.7)$$

where γ_d is a constant. This leads to a drag which in the absence of critical level effects (see section 10.3) exerts the same force per unit mass at all levels, since from the hydrostatic equation

$$\frac{1}{\rho}\frac{\partial\tau}{\partial z} = g\frac{\partial\tau}{\partial p}. \quad \ldots (10.8)$$

The gravity-wave drag is applied between the top of the boundary layer and the critical level beyond which the waves are assumed to be unable to propagate. The constant γ_d may be calculated by ignoring the effects of this critical level. Since the surface flux must be totally absorbed by the atmosphere:

$$\tau_* = \int_0^{p_*} \frac{\partial\tau}{\partial p}\,dp \quad \ldots (10.9)$$

and since $\partial\tau/\partial p = 0$ (by assumption) within the boundary layer

$$\tau_* = \sum_{k=b+1}^{\text{TOP}} \gamma_d \Delta p_k = \gamma_d p_{b+\frac{1}{2}} \quad \ldots (10.10)$$

where b is the number of levels in the model boundary layer. Therefore at level k

$$\frac{1}{\rho_k}\frac{\Delta\tau_k}{\Delta z_k} = -\frac{g\tau_*}{p_{b+\frac{1}{2}}}. \quad \ldots (10.11)$$

In operational use $\tau_* = 0.15\,\text{N m}^{-2}$.

10.3. *Treatment of the critical level*

The gravity waves are assumed to propagate vertically until they reach a critical level, k_{crit} at which they are either absorbed or reflected. This occurs at a reversal in direction of a wind component (Booker and Bretherton 1967) for stationary waves. The u and v components of the wind field are treated independently in this scheme. The wave momentum flux carried by a particular component is considered unable to propagate beyond this level and 50% is absorbed. The remainder is assumed to be reflected and is ignored. If a critical level occurs below the first level at which the waves begin to dissipate, no drag is calculated.

At and above level k_{crit}, no drag is applied. The effects of the critical level are only applied at level $k_{crit}-1$. At this level

$$\Delta\tau_{k_{crit}-1} = -(1-\beta)\tau_{k_{crit}-\frac{3}{2}} = -(1-\beta)\frac{\tau_* p_{k_{crit}-\frac{3}{2}}}{p_{b+\frac{1}{2}}} \quad \ldots (10.12)$$

where $\beta = \frac{1}{2}$ is the coefficient of reflection. It then follows that

$$-\frac{1}{p_{k_{crit}-1}}\frac{\Delta\tau_{k_{crit}-1}}{\Delta z_{k_{crit}-1}} = \frac{-(1-\beta)g\tau_* p_{k_{crit}-\frac{3}{2}}}{\Delta p_{k_{crit}-1}\, p_{b+\frac{1}{2}}} \quad \ldots (10.13)$$

11. STABILITY AND ZONAL FILTERING

A major problem with the regular latitude–longitude grid chosen for the model is that, due to the convergence of the meridians, the zonal separation of grid points decreases as the poles are approached. Thus, according to the Courant–Friedrichs–Lewy (CFL) stability criterion, a very short time-step is required in order to maintain computational stability at these high latitudes. For the global version of the model, for example, the adjustment time-step would need to be less than 18 seconds, making this model far too expensive to integrate.

A linear stability analysis shows that only certain wavelengths are unstable for a given grid length and unstable time-step. These are waves shorter than a critical number of grid lengths. The problem is therefore solved by using a long time-step and removing these wavelengths by applying a zonal filter, thereby increasing the effective zonal separation of the grid points without sacrificing the regularity of the grid.

The time-step is chosen to ensure that the model is both stable and economical, taking into account the computational expense of the zonal filter and the loss in effective longitudinal resolution as the filtering region is extended equatorwards. An adjustment time-step of 5 minutes is used in the coarse-mesh model. This is stable equatorwards of latitude 60° with the resolution used. The advection step of 15 minutes is also stable within this region provided that the maximum wind speed, u_{MAX}, is less than 116 m s^{-1} (see Table XII).

11.1. *Fourier damping in the coarse-mesh model*

Early versions of the global and hemispheric models used a Fourier chopping technique (Williamson 1976) to maintain stability at high latitudes. This has now been superseded by a Fourier damping technique, which selectively damps rather than discards all unstable wave components.

The reason for replacing chopping by damping is the discontinuous nature of chopping. At each model latitude there is a transition from the total retention to the total exclusion of a component in wave-number space. This acts as an internal boundary which can reflect waves. Such an effect is undesirable and makes the model more susceptible to numerical instability. It can also lead to inaccurate results. Hills (1982) has shown that it can lead to the generation of unrealistic features at high latitudes.

TABLE XII. *The maximum stable wind speed* ($m\,s^{-1}$) *predicted by linear theory for the advection step of the coarse-mesh model*

Δt	Latitude 45°	60°	80°
minutes			
10	246	174	60
15	164	116	40
20	123	87	30

TABLE XIII. *The weighting coefficient used for calculating the filtered field,* $\theta' = \omega T + (1 - \omega)\theta$

Level	ω
10–15	1.0
5–9	0.5
1–4	0.0

In the forecast model, Fourier damping is carried out in the region polewards of a predetermined latitude, $\tilde{\phi}$. For each latitude $\phi > \tilde{\phi}$, Fourier coefficients are obtained by applying the discrete Fourier transform:

$$\tilde{X}_j(\phi, \sigma_N) = \frac{1}{N} \sum_{k=0}^{N-1} X(\lambda_k, \phi, \sigma) e^{-ij\lambda_k} \qquad \ldots (11.1)$$

where N is the number of points around a latitude circle, $-\frac{1}{2}N < j < \frac{1}{2}N + 1$ and $\lambda_k = 2\pi k/N$. X is a model prognostic variable. Each wave-number coefficient is then multiplied by a damping factor, $\alpha(\lambda_j)$, such that their product is less than unity, and the filtered field X' reconstructed using

$$X'(\lambda_k, \phi, \sigma) = \sum_{j=-\frac{1}{2}N}^{\frac{1}{2}N+1} \alpha(\lambda_j) \tilde{X}_j(\phi, \sigma) e^{ik\lambda_j}. \qquad \ldots (11.2)$$

The damping factor, $\alpha(\lambda_j)$, is the reciprocal of the linear amplification factor $A(\lambda_j)$ derived from the linear analysis of the adjustment (adj) and advection (adv) steps

$$A(\lambda_j) = \max\{\gamma_s A_{\text{adj}}(\lambda_j), \gamma_s A_{\text{adv}}(\lambda_j), 1\}. \qquad \ldots (11.3)$$

γ_s is a constant factor to allow for reduced stability due to non-linear effects. At present a value of $\gamma_s = 1.1$ is used.

The filter is applied to all prognostic variables at the end of each adjustment and advection step. Special measures are required for those variables that vary slowly at constant pressure but rapidly with pressure since filtering along σ-surfaces over steep orography will give undesirable results. The scheme therefore filters the prognostic variables u, v and q together with Δp_* (the surface pressure increment) and a linear combination of θ and

$T, \theta' = \omega T + (1 - \omega)\theta$. The value of ω varies with height so that θ is filtered near the ground and T is filtered at upper levels. ω is tabulated in Table XIII. The σ values of the levels specified in this table have been given in Table I.

The model allows the amount of damping taking place at a given latitude to be automatically adjusted by the forecast as it progresses. This ensures that only the minimum necessary filtering is performed whilst at the same time allowing the model to respond to any significant increase in zonal wind speed. Each hemisphere is treated separately. In general, more model latitudes will be filtered in the winter hemisphere and these will be damped more strongly.

The maximum zonal wind speed, $u_{\max}$, occurring between the equator and the current model row is used to determine whether damping takes place. Thus, from the CFL stability criterion, damping is performed if

$$\max(\gamma_s^2 u_{\mathrm{MAX}}^2, \gamma_s^2 c^2 \Delta t^2/\delta t^2) > 1 \qquad \ldots (11.4)$$

where c is the phase speed of the fastest-moving gravity wave, Δt is the advection time-step and δt is the adjustment time-step.

11.2. *Multipoint filtering in the fine-mesh model*

The zonal periodicity required for the direct application of the Fourier transform is not present in the fine-mesh model because of the restricted nature of its forecast domain. An alternative method to the one described above must therefore be sought.

The chosen approach uses a multipoint filtering technique based on the ideas of Hills (1982). A local approximation to the Fourier transform is used to construct a filter of the form

$$\Delta X'_k = \sum_{m=-M}^{M} c_m \Delta X_{k+m} \qquad \ldots (11.5)$$

where M is the half-width of the filter and ΔX represents the increment being added to the model fields (Δu, Δv, Δp_*, Δq or $\Delta\theta$). A value of $M = 12$ is used operationally.

The coefficients $c_{-M} \ldots c_M$ are constants for a given latitude and are calculated from the amount of damping required for linear stability. This method has a similar effect to the Fourier damping method employed in the coarse-mesh model, reducing the amplitude of each wave by the amount of unstable amplification. The increments ΔX are assumed to be zero outside the east–west lateral boundaries of the model so that the filter may be applied near the edges of the forecast area.

The coefficients $c_{-M} \ldots c_M$ are determined by taking an inverse Fourier transform of the form

$$c_m = \frac{1}{N} \sum_{j=-\frac{1}{2}N}^{\frac{1}{2}N+1} \frac{1}{A(\lambda_j)} e^{im\lambda_j} \qquad \ldots (11.6)$$

where $|m| < M$, N is the number of points around a latitude circle, using the zonal grid separation of the fine-mesh model, and A is an amplification factor predicted by linear

theory. The values produced by solving equation (11.6) are then adjusted so that

$$\sum_{m=-M}^{M} c_m = 1 \qquad \ldots (11.7)$$

in order that the mean value along a row is conserved by the filter.

The amplification factor is given by equation (11.3). A higher value of $\gamma_s = 1.2$ is used for the fine-mesh model in order to compensate for the approximate modelling of the filter's response due to the truncation of the Fourier series.

12. LATERAL BOUNDARY CONDITIONS AND THE TREATMENT OF THE POLES

12.1. *Fine-mesh model*

In the fine-mesh model, which covers a restricted geographical area, the boundaries can influence the synoptic behaviour over the whole forecast region in a short time. It is therefore necessary to impose boundary conditions which allow the movement of synoptic features through the edges of the forecast region.

This is done by extracting values of the prognostic variables p_*, θ, q, u and v from a coarse-mesh forecast at hourly intervals and linearly interpolating these to the corresponding fine-mesh boundary points. These are then converted into tendencies. The fine-mesh boundaries are updated using these tendencies every advection time-step. Thus, for any variable X ($= u, v, \theta, q$ or p_*)

$$X_c^{n+1} = X_b^n + \Delta t \left(\frac{\partial X_b}{\partial t} \right)_c^n \qquad \ldots (12.1)$$

where suffix b refers to boundary values and suffix c refers to values interpolated from the coarse-mesh model.

A region of high diffusion is imposed around the edges of the fine-mesh area to smooth any roughnesses caused by inconsistencies between the fine-mesh and coarse-mesh forecasts. This enhanced diffusion zone is three grid lengths deep. The value of the diffusion coefficient varies with latitude but is typically three times the value used in the interior of the forecast region.

Experience has shown that it is advisable to ensure that the coarse-mesh forecast used to generate the boundary conditions for a fine-mesh forecast starts from the same analysis as the fine-mesh forecast. If this is not done there can be pressure oscillations leading to large-scale changes in the fine-mesh forecast. For this reason a 48-hour hemispheric forecast is used to generate the boundary tendencies required for the 12 hours of fine-mesh assimilation and a 36-hour fine-mesh forecast.

12.2. *The treatment of the poles*

In the coarse-mesh model the variables p_*, θ and q are stored at the poles. At each time-step

their values are set equal to the mean of the surrounding points. Thus the surface pressure at the poles, p_*^P, is given by

$$p_*^P = \frac{1}{N}\sum_{n=1}^{N}(p_*^A)_n \qquad \ldots (12.2)$$

where N is the number of model points in the east–west direction and the superscript A refers to the values on the row adjacent to the pole.

The above procedure cannot be directly applied to the values of the wind field (u, v), since they are stored a half grid length away from the pole. Instead a mean cartesian wind is first calculated at the pole and this is then used to compute new values of u, v. Hence at the northernmost row for $m = 1 \ldots N$

$$\left.\begin{aligned} u_m &= \frac{1}{N}\sum_{n=1}^{N}(u_n^A\cos\gamma_n - v_n^A\sin\gamma_n)\cos\gamma_m + \frac{1}{N}\sum_{n=1}^{N}(u_n^A\cos\gamma_n + v_n^A\sin\gamma_n)\sin\gamma_m \\ v_m &= \frac{1}{N}\sum_{n=1}^{N}(u_n^A\cos\gamma_n + v_n^A\sin\gamma_n)\cos\gamma_m - \frac{1}{N}\sum_{n=1}^{N}(u_n^A\cos\gamma_n - v_n^A\sin\gamma_n)\sin\gamma_m \end{aligned}\right\} \ldots (12.3)$$

where $\gamma_m = 2\pi m/N$.

12.3. *The southern boundary in hemispheric forecasts*

The values of the prognostic variables are kept constant along the southern boundary during hemispheric forecasts. The mean meridional velocity at the southern boundary is constrained to be zero by initially setting

$$v'_m = v_m - \frac{1}{N}\sum_{n=1}^{N} v_n$$

for $m = 1 \ldots N$. This ensures that there is no net mass through the boundaries.

ACKNOWLEDGEMENTS

The development and implementation of the operational numerical weather prediction scheme has involved a large number of people in the Forecasting Research Branch and the Central Forecasting Branch of the Meteorological Office. In particular we would like to acknowledge the contribution of Dr P. W. White who led the project, Dr T. Davies and Dr M. J. P. Cullen who made significant contributions to the development of the forecast model and Dr W. H. Lyne who designed the data assimilation scheme. The physical parametrizations used in the model are based on schemes originally designed by members of the Dynamical Climatology Branch of the Meteorological Office for use in their General Circulation Model and we would like to acknowledge their continuing assistance.

BIBLIOGRAPHY

ARAKAWA, A.; 1966, Computational design for long-term numerical integration of the equations of fluid motion: two-dimensional incompressible flow. Part 1. *J Comput Phys*, **1**, pp. 119–143.

——; 1969, Parameterization of cumulus convection. Proceedings of the WMO/IUGG Symposium on Numerical Weather Prediction in Tokyo November 26–December 4, 1968. Japan Met Agency, Tech Report No. 67, pp. iv-8-1–iv-8-6.

BENNETTS, D. A. and RAWLINS, F.; 1981, Parametrization of the ice-phase in a model of mid-latitude cumulonimbus convection and its influence on the simulation of cloud development. *Q J R Meteorol Soc*, **107**, pp. 477–502.

BLACKADAR, A. K.; 1975, High resolution models of the planetary boundary layer. EPA-SRG Annual Report 1975, Contribution from Pennsylvania State University.

BOLTON, J. A.; 1981, The estimation of zonally averaged climatological cloud data for use in the 5 level model radiation scheme. (Unpublished, copy available in the National Meteorological Library, Bracknell.)

BOOKER, J. R. and BRETHERTON, F. P.; 1967, The critical layer for internal gravity waves in a shear flow. *J Fluid Mech*, **27**, pp. 513–539.

BRETHERTON, F. P.; 1969, Momentum transport by gravity waves. *Q J R Meteorol Soc*, **95**, pp. 213–243.

BURRIDGE, D. M. and GADD, A. J.; 1977, The Meteorological Office operational 10-level numerical weather prediction model (December 1975). *Sci Pap, Meteorol Off*, No. 34.

CARPENTER, K. M.; 1977, Surface exchanges in a mesoscale model of the atmosphere. (Unpublished, copy available in the National Meteorological Library, Bracknell.)

——; 1981, The accuracy of Gadd's modified Lax–Wendroff algorithm for advection. *Q J R Meteorol Soc*, **107**, pp. 467–470.

CARSON, D. J.; 1982, Current parameterizations of land-surface processes in atmospheric general circulation models. *In* EAGELSON, P. S. (ed.), Land surface processes in atmospheric general circulation models, Cambridge University Press, pp. 67–108.

CARSON, D. J. and RICHARDS, P. J. R.; 1978, Modelling surface turbulent fluxes in stable conditions. *Boundary-layer Meteorol*, **14**, pp. 67–81.

CESELSKI, B. F.; 1972, A comparison of cumulus parameterization techniques in numerical integrations of an easterly wave, Report 4 in numerical weather prediction over the tropics. Report No. 72-1, Department of Meteorology, Florida State University, Tallahassee.

CULLEN, M. J. P., FOREMAN, S. J., PRINCE, J. W., RADFORD, A. M. and ROSKILLY, D. R.; 1981, Forecast intercomparisons of three numerical weather prediction models from the UK Meteorological Office. *Mon Weather Rev*, **109**, pp. 422–452.

DALEY, R.; 1980, On the optimal specification of the initial state for deterministic forecasting. *Mon Weather Rev*, **108**, pp. 1719–1735.

DAVIES, H. C. and TURNER, R. E.; 1977, Updating prediction models by dynamical relaxation: an examination of the technique. *Q J R Meteorol Soc*, **103**, pp. 225–245.

DEY, C. H.; 1978, Noise suppression in a primitive equation prediction model. *Mon Weather Rev*, **106**, 159–173.

DYER, A. J. and HICKS, B. B.; 1970, Flux-gradient relationships in the constant flux layer. *Q J R Meteorol Soc*, **96**, pp. 715–721.

FRITTS, D. C.; 1984, Gravity wave saturation in the middle atmosphere: A review of theory and observations. *Rev Geophys and Space Phys*, **22**, pp. 275–308.

GADD, A. J.; 1978a, A split explicit integration scheme for numerical weather prediction. *Q J R Meteorol Soc*, **104**, pp. 569–582.

——; 1978b, A numerical advection scheme with small phase speed errors. *Q J R Meteorol Soc*, **104**, pp. 583–594.

——; 1980, Two refinements of the split explicit integration scheme. *Q J R Meteorol Soc*, **106**, pp. 215–220.

GANDIN, L. S.; 1963, The objective analysis of meteorological fields. Izdatel, Leningrad. (Translated by the Israel Program for Scientific Translations, Jerusalem, 1968.)

GHIL, M., HALEM, M. and ATLAS, R.; 1979, Time-continuous assimilation of remote-sounding data and its effect on weather forecasting. *Mon Weather Rev*, **107**, pp. 140–171.

GILCHRIST, A. and WHITE, P. W.; 1982, The development of the Meteorological Office new operational forecasting system. *Meteorol Mag*, **111**, pp. 161–179.

GOODY, R. M.; 1964, Atmospheric radiation: I theoretical basis. Oxford University Press.

HAYDEN, C. M.; 1973, Experiments in the four-dimensional assimilation of Nimbus 4 SIRS data. *J Appl Meteorol*, **12**, pp. 425–436.

HICKS, B. B.; 1976, Wind profile relationships from the 'Wangara' experiment. *Q J R Meteorol Soc*, **102**, pp. 535–551.

HILLS, T. S.; 1982, The use of a numerical filter to control stability in a general circulation model. (Unpublished, copy available in the National Meteorological Library, Bracknell.)

HOKE, J. E. and ANTHES, R. A.; 1976, The initialization of numerical models by a dynamic-initialization technique. *Mon Weather Rev*, **104**, pp. 1551–1556.

HOUGHTON, J. T.; 1963, The absorption of solar infra-red radiation by the lower stratosphere. *Q J R Meteorol Soc*, **89**, pp. 319–331.

——; 1977, The physics of atmospheres. Cambridge University Press.

HUNT, G. E. and MATTINGLY, S. R.; 1976, Infrared radiative transfer in planetary atmospheres—I. Effects of computational and spectroscopic economies on thermal heating/cooling rates. *J Quant Spectrosc Radiat Transfer*, **16**, 505–520.

JANJIC, Z. I.; 1979, The forward-backward scheme modified to prevent two-grid-interval noise and its application in σ coordinate models. *Contrib Atmos Phys*, **52**, pp. 69–84.

KISTLER, R. E. and MCPHERSON, R. D.; 1975, On the use of a local wind correction technique in four-dimensional data assimilation. *Mon Weather Rev*, **103**, pp. 445–449.

KITCHEN, J. E., CARTER, M. J. and DAY, A. P.; 1985, Results of a trial of a parametrization of gravity wave drag in the operational forecast model. (Unpublished, copy available in the National Meteorological Library, Bracknell.)

LILLY, D. K.; 1972, Wave momentum flux—a GARP problem. *Bull Am Meteorol Soc*, **53**, pp. 17–23.

LIOU, K.-N.; 1980, An introduction to atmospheric radiation. International Geophysical Series, **26**, New York, Academic Press.

LIU, J. V. and ORVILLE, H. D.; 1969, Numerical modelling of precipitation and cloud shadow effects on mountain-induced cumuli. *J Atmos Sci*, **26**, pp. 1283–1298.

LORENC, A. C.; 1976, Results of some experiments assimilating observations from a simulation of the FGGE observing system into a global general circulation model; JOC Study Group Conference on four-dimensional data assimilation. GARP Programme on Numerical Experimentation Report No. 11, pp. 358–374.

——; 1981, A global three-dimensional multivariate statistical interpolation scheme. *Mon Weather Rev*, **109**, pp. 701–721.

LUDLAM, F. H.; 1963, Severe local storms: a review. *Meteorol Monogr*, **5**, pp. 1–30.

——; 1980, Clouds and storms, Pennsylvania, State University Press.

LYNE, W. H.; 1979, Data assimilation by repeated correction of model fields—theoretical considerations. (Unpublished, copy available in the National Meteorological Library, Bracknell.)

LYNE, W. H. and ROWNTREE, P. R.; 1976, Development of a convective parameterisation using GATE data. (Unpublished, copy available in the National Meteorological Library, Bracknell.)

LYNE, W. H., SWINBANK, R. and BIRCH, N. T.; 1982, A data assimilation experiment and the global circulation during the FGGE special observing periods. *Q J R Meteorol Soc*, **108**, pp. 575–594.

MANABE, S. and MÖLLER, F.; 1961, On the radiative equilibrium and heat balance of the atmosphere. *Mon Weather Rev*, **89**, pp. 503–532.

MESINGER, F.; 1973, A method for construction of second order accuracy difference schemes permitting no false two-grid-interval wave in the height field. *Tellus*, **25**, pp. 444–458.

MIYAKODA, K., STRICKLER, R. F. and CHLUDZINSKI, J.; 1978, Initialization with the data assimilation method. *Tellus*, **30**, pp. 32–54.

MONIN, A. S. and OBUKHOV, A. M.; 1954, Basic regularity in turbulent mixing in the surface layer of the atmosphere. *Akad Nauk SSSR Geofiz Inst Transl* No. 24 (151), pp. 163–187.

MONTEITH, J. L.; 1973, Principles of environmental physics. London, Arnold.

PALMER, T. N., SHUTTS, G. J. and SWINBANK, R.; 1986, Alleviation of a systematic westerly bias in general circulation and numerical weather prediction models through an orographic gravity wave drag parametrization. *Q J R Meteorol Soc*, **112**, pp. 1001–1039.

PHILLIPS, N. A.; 1957, A coordinate system having some special advantages for numerical forecasting. *J Meteorol*, **14**, pp. 184–185.

PRIESTLEY, C. H. B. and TAYLOR, R. J.; 1972, On the assessment of surface heat flux and evaporation using large-scale parameters. *Mon Weather Rev*, **100**, pp. 81–92.

RICHARDS, P. J. R.; 1980, The parametrization of boundary layer processes in general circulation models. (Ph.D. thesis, University of Reading.)

RIEHL, H.; 1954, Tropical meteorology, New York, McGraw-Hill.

ROBERTS, R. E., SELBY, J. E. A. and BIBERMAN, L. M.; 1976, Infrared continuum absorption by atmospheric water vapor in the 8–12-μm window. *Appl Optics*, **15**, pp. 2085–2090.

ROTHMAN, L. S.; 1981, AFGL atmospheric absorption line parameters compilation: 1980 version. *Appl Optics*, **20**, pp. 791–795.

ROWNTREE, P. R.; 1983, Land surface processes in climate models—parametrization and model sensitivity. (Unpublished, copy available in the National Meteorological Library, Bracknell.)

RUTHERFORD, I. D.; 1972, Data assimilation by statistical interpolation of forecast error fields. *J Atmos Sci*, **29**, pp. 809–815.

SAWYER, J. S.; 1960, Numerical calculation of the displacements of a stratified airstream crossing a ridge of small height. *Q J R Meteorol Soc*, **86**, pp. 326–345.

SCORER, R. S.; 1958, Natural aerodynamics, London, Pergamon Press.

SLINGO, A.; 1985, Handbook of the Meteorological Office 11-layer atmospheric general circulation model. (Unpublished, copy available in the National Meteorological Library, Bracknell.)

SLINGO, J. M.; 1980, A cloud parametrization scheme derived from GATE data for use with a numerical model. *Q J R Meteorol Soc*, **106**, pp. 747–770.

SLINGO, A. and WILDERSPIN, R. C.; 1984, Development of a revised longwave radiation scheme for an atmospheric general circulation model. (Unpublished, copy available in the National Meteorological Library, Bracknell.)

WARRILOW, D. A., SANGSTER, A. B. and SLINGO, A.; 1986, Modelling of land surface processes on European climate. (Unpublished, copy available in the National Meteorological Library, Bracknell.)

WEBB, E. K.; 1970, Profile relationships: The log-linear range, and extension to strong stability. *Q J R Meteorol Soc*, **96**, pp. 67–90.

WILLIAMSON, D. L.; 1976, Linear stability of finite-difference approximations on a uniform latitude-longitude grid with Fourier filtering. *Mon Weather Rev*, **104**, 31–41.

WOODAGE, M. J.; 1985, The preparation of data for the Meteorological Office operational 15-level forecast model. *Meteorol Mag*, **114**, pp. 1–13.

Printed in the United Kingdom for Her Majesty's Stationery Office
Dmd 0240017 9/87 C9 3379 28940

HMSO publications are available from:

HMSO Publications Centre
(Mail and telephone orders only)
PO Box 276, London, SW8 5DT
Telephone orders 01-622 3316
General enquiries 01-211 5656
(queuing system in operation for both numbers)

HMSO Bookshops
49 High Holborn, London, WC1V 6HB 01-211 5656 (Counter service only)
258 Broad Street, Birmingham, B1 2HE 021-643 3740
Southey House, 33 Wine Street, Bristol, BS1 2BQ (0272) 264306
9–21 Princess Street, Manchester, M60 8AS 061-834 7201
80 Chichester Street, Belfast, BT1 4JY (0232) 238451
71 Lothian Road, Edinburgh EH3 9AZ 031-228 4181

HMSO's Accredited Agents
(see Yellow Pages)

and through good booksellers

£9.75 net

ISBN 0 11 400354 8